Inhibitory interneurons within the deep dorsal horn integrate convergent sensory input to regulate motor performance

Authors

Nofar Ozeri-Engelhard*[1,2,3,6,7], Mark A Gradwell*[1,2,6,7], Olivier D Laflamme[4,5], Aman Upadhyay[1,2,3], Adin Aoki[1,2], Tara Shrier[1,2], Melissa Gandhi[1,2], Melissa Gonzalez[2], Jaclyn T Eisdorfer[1,2], Gloria Abbas- Zadeh[1,2], Nusrath Yusuf[1,2,3], Jordan Katz[1,2], Michael Haas[1,2], Turgay Akay[5], Victoria Abraira[1,2]

* These authors have contributed equally

[1]Cell Biology and Neuroscience Department, Rutgers University, The State University of New Jersey, New Brunswick, United States of America
[2]W.M. Keck Center for Collaborative Neuroscience, Rutgers University, The State University of New Jersey, New Brunswick, United States of America
[3]Neuroscience PhD program at Rutgers Robert Wood Johnson Medical School, Piscataway, New Jersey, United States of America
[4]Dalhousie PhD Program
[5]Dalhousie University, Dept. of Medical Neuroscience, Atlantic Mobility Action Project, Brain Repair Center, Halifax, NS, Canada
[6]equal contribution
[7]lead contact

Correspondence

victoria.abraira@rutgers.edu (V.E.A)

Highlights

- Inhibitory interneurons in the medial deep dorsal horn (mDDH), a “hot zone” of convergence cutaneous and proprioceptive inputs, are preferentially recruited during locomotion.

- We identified an inhibitory population of Glycinergic deep dorsal horn parvalbumin-expressing interneurons (dPVs) which are active during locomotion, integrate multimodal sensory inputs, and target motor networks.

- Ablation of dPVs reveals a state and phase- dependent role in modulation of locomotion parameters and kinematics.

- Electromyogram recordings demonstrate that dPVs modulate the cutaneous-evoked response in hindlimb muscles, establishing them as the first genetically identified inhibitory neurons in a cutaneous- motor pathway.

SUMMARY

To achieve smooth motor performance in a rich and changing sensory environment, motor output must be constantly updated in response to sensory feedback. Although proprioception and cutaneous information are known to modulate motor output, it is unclear whether they work together in the spinal cord to shape complex motor actions such as locomotion. Here we identify the medial deep dorsal horn (mDDH) as a “hot zone” of convergent proprioception and cutaneous input for locomotion. Due to increased responsiveness to sensory input, inhibitory interneurons in the mDDH area are preferentially recruited in locomotion. To study inhibitory interneurons in this area, we utilize an intersectional genetic strategy to isolate and ablate a population of parvalbumin-expressing glycinergic interneurons in the mDDH (dPVs). Using histological and electrophysiological methods we find that dPVs integrate proprioceptive and cutaneous inputs while targeting ventral horn motor networks, suggesting a role in multimodal sensory processing for locomotion. Consistent with this, dPVs ablation alters step cycle parameters and kinematics in a speed and phase dependent manner. Finally, we use EMG muscle recordings to directly show that dPVs are part of a cutaneous-motor pathway. Our results indicate that dPVs form a critical node in the spinal sensorimotor circuitry.

INTRODUCTION

The ability to locomote is fundamental to almost every living creature, making it one of the most robust motor behaviors across the animal kingdom. Whether by searching for food, escaping a predator, or migrating due to climate change, animals use locomotion for survival. It is thus not surprising that the study of locomotion can be dated back to Aristotle, among other philosophers and Greek physicians during the 3rd century (*Aristotle’s De Motu Animalium* 1986). However, it was the experiments performed by Charles Sherrington and Graham Brown during the 20th century that shaped our current views about the circuits involved in locomotion. Sherrington proposed that locomotion is organized as a “chain” of reflexes, requiring the participation of sensory feedback (C. S. Sherrington 1906). However, Brown’s pioneering experiments, recording fictive locomotion in decerebrated and deafferented cats, demonstrated that locomotion persists in the absence of sensory feedback (T. G. Brown and Sherrington 1911). These studies led to the dogma most accepted today of “Central Pattern Generator” (CPGs), intrinsic spinal networks generating the rhythmic and alternating activity controlling locomotion. Although not required for its generation, sensory input plays an important role in locomotion. In humans, permanent loss of large sensory fibers leads to a complete inability to walk, which is only regained following long training and visual guidance (Lajoie et al. 1996; Tuthill and Azim 2018). Further, robots that incorporate the principles of CPGs alone, fail to adjust their walk to changes in terrain or perturbations.

Two main sensory inputs “disturb” the rhythmic pattern of locomotion. The first is proprioception, the sense of one’s own body position and movement, detected by receptors embedded in muscles, joints, and tendons. The second is cutaneous input, relaying information about skin distortion and detected by low threshold mechanoreceptors (LTMRs) innervating it. Studies show that both proprioceptive and cutaneous afferents can initiate, arrest, reset, and enhance locomotion (C. Sherrington 1910; Grillner and Rossignol 1978; J and Kg 1980). Further,

experiments evoking proprioceptive or cutaneous reflexes during locomotion demonstrate changed muscle response. For example, inducing the stumbling reflex with mechanical perturbations to the dorsum of the foot, triggers knee flexion followed by flexion of the ankle and hip to clear the obstacle and place the foot in front of it (Forssberg 1979). Similar experiments (Schillings, Van Wezel, and Duysens 1996; Forssberg, Grillner, and Rossignol 1975) , as well as modeling studies (Prochazka and Yakovenko 2007 conclude that the main role of proprioceptive and cutaneous input is in tuning locomotion to kinematics requirements and environmental changes.

For efficient modulation of locomotion, information from both proprioceptors and cutaneous receptors must be integrated and processed by motor networks. In the cat spinal cord, the medial part of the deep dorsal horn (DDH) was found to be an area of convergent proprioceptive and cutaneous inputs, suggesting that interneurons (INs) located in this area process multimodal sensory input for locomotion. Additionally, the same area was identified in the mouse as a hot zone of premotor interneurons, indicating these INs might participate in multimodal sensorimotor processing.

Over the last decade, striking progress in the development of mouse genetic tools enabled precise access to spinal cord interneuron populations defined by their common gene expression (Abraira et al. 2017). Using these tools, both excitatory and inhibitory DDH INs were found to perform multimodal sensorimotor processing. For example, the excitatory dI3 pre-motor interneuron integrates proprioceptive and LTMR input, and regulates grasping in response to a change in environment (Bui et al. 2013). Inhibitory neurons expressing the satb2 transcription factor integrate proprioception and nociception and play an appropriate role in modulation of locomotion and pain withdrawal reflex (Hilde et al. 2016). Inhibitory RorB expressing neurons mainly integrate proprioceptive input and modulate locomotion in a phase dependent manner by exerting presynaptic inhibition on proprioceptive afferents (Koch et al. 2017).

While we have a better understanding of the role of DDH INs in sensorimotor control, a broader characterization of this area, as well as identification of new uncharacterized populations is still lacking. Here we find that the highest convergence of proprioception and cutaneous input in the mouse is localized to the medial portion of laminas 4-5 (laminas 4-5m). Although excitatory INs in this region receive a stronger sensory input, inhibitory INs are more ready to respond and indeed, are preferentially recruited during locomotion. We then hone down on the laminae 4-5m parvalbumin-expressing INs (dPVs) and hypothesize that they integrate multimodal sensory input and relay it to spinal cord motor networks to modulate locomotion. With colocalization experiments, we show that dPVs represent a new and uncharacterized population, originating from the dorsal Lbx1 lineage. dPVs circuit connectivity, characterized by histology and functional assays, support a role in sensorimotor processing. Following dPVs ablation, EMG muscle recordings reveal a loss of cutaneous evoked -inhibition. With a battery of behavior assays, we show that dPVs' ablation affects mice behavior in a task, speed, and phase dependent manner. Rotarod, balance beam and ladder performance are mostly unaffected. On the other hand, during high speed, but not low speed treadmill locomotion, mice show smaller strides and increased stride frequency. Kinematic analysis reveals hyperflexion of limb joints during stance, but not swing. Further, changes in forelimb-hindlimb interlimb coordination result in altered gait

transitions to high speed associated gaits.

In summary, here we genetically identify DDH parvalbumin INs (dPVs), characterize their electrophysiological properties and input- output connectivity that underlie a phase and state dependent role in locomotion.

RESULTS

The medial deep dorsal horn is defined by convergent proprioceptive and cutaneous input

Integration of proprioceptive and cutaneous information is essential to normal locomotion and motor adaptation. To identify spinal regions that process convergent proprioceptive and cutaneous inputs, we first visualized the terminal endings of these populations using *PV*^{2aCreER};*Advillin*^{FlpO};*Rosa*$^{LSL\text{-}FSF\text{-}TdTomato}$;*Rosa*$^{LSL\text{-}SynGFP}$ mice (**Figure 1A-B**). We found that cutaneous inputs (green) are restricted to the superficial and deep dorsal horn (LI-IV), while proprioceptive inputs (yellow) span the deep dorsal and ventral horns (LIV-X). Of particular interest, convergent sensory input (green + yellow) was largely restricted to the medial deep dorsal horn (mDDH) (**Figure 1B**). This finding suggests that the mDDH plays an important role in integrating convergent proprioceptive and cutaneous sensory inputs.

We next sought to determine the spinal regions activated by tasks requiring proprioceptive and cutaneous sensory input. To address this (**Figure 1C**), we examined the expression of the early immediate gene c-fos, used as a correlate of neuronal activity (Hunt, Pini, and Evan 1987; Morgan and Curran 1986), during rest, swim (integrating predominantly proprioceptive), and walk (integrating proprioceptive and cutaneous) (Muir and Steeves 1995; Gruner and Altman 1980).

During walking, recruiting both proprioceptive and cutaneous sensory inputs (Muir and Steeves 1995; Gruner and Altman 1980), we observed a an increase in c-fos positive neurons throughout the deep and ventral laminas, particularly within the medial region of LIV-V (**Figure 1D-F**). Together, these data highlight the mDDH as a unique region activated by convergent sensory input from proprioceptive and cutaneous primary afferents.

Deep dorsal horn inhibitory neurons exhibit preferred excitability and responsiveness to sensory input

Given that inhibitory and excitatory neurons are functionally divergent, we separately examined their c-fos expression in the DDH, using *vGAT*^{Cre};*Tau*$^{LSL\text{-}LacZ}$ mice. Quantification of c-fos in inhibitory (c-fos^{+}/LacZ^{+}) and excitatory (c-fos^{+}/LacZ^{-}) neurons suggested that increased c-fos expression following swim and walk is attributed to enhanced activity in inhibitory, but not excitatory neurons (**Figure 2A-C)**. In line with enhanced inhibitory neuron recruitment during sensorimotor behavior, we found that optogenetic activation of sensory afferents (**Figure 2D)** is more likely to evoke APs in inhibitory neurons than excitatory neurons (**Figure 2E)**, despite

receiving similar amplitude inputs (**Figure 2F**). The preferred recruitment of inhibitory neurons suggests distinct roles for DDH excitatory and inhibitory neurons, with a prevalent role for inhibition in sensorimotor control.

To further explore the functional properties of these two populations, we performed an electrophysiological characterization of randomly sampled excitatory and inhibitory neurons within the DDH using the *vGluT2*^{Cre}*;Rosa*$^{LSL\text{-}TdTomato}$ and *vGAT*^{Cre}*;Rosa*$^{LSL\text{-}TdTomato}$ lines, respectively (**Figure 2G**). Cell-attached recordings showed that while the majority of inhibitory neurons are spontaneously active (sAP), significantly fewer excitatory neurons exhibit sAP discharge (**Figure 2H-I**). Of the spontaneously active neurons, inhibitory neurons showed higher sAP frequency with a lower coefficient of variation (**Figure 2J-K**). Increased AP discharge in response to sensory input, without any difference in input amplitude, and increased sAP discharge suggest that inhibitory neurons exhibit more excitable intrinsic properties than their excitatory counterparts.

To better understand how excitatory and inhibitory interneurons integrate information, we characterized their intrinsic electrophysiological properties. Using previously established AP discharge phenotypes (Browne et al. 2020), we found the majority of excitatory and inhibitory neurons within the DDH exhibit TF AP discharge patterns in response to depolarizing current injection (**Figure 2F**, **Figure S1A**). TF INs could be further classified into 2 subcategories: TF-non-accommodating (TF_{Na}) and TF accommodating (TF_{Ac}). TF_{Na} was more frequently observed in inhibitory neurons whereas TF_{Ac} and DF were more frequently observed in excitatory neurons (**Figure S1A**). These discharge patterns are consistent with increased AP threshold adaptation in excitatory neurons (**Figure S1B**). In response to depolarizing current injection, inhibitory neurons showed a lower latency to the first AP (**Figure 2M**), an increased number of APs (**Figure 2N**),and increased instantaneous AP frequency (**Figure S1C**). When examining AP properties, we found significant differences in AP threshold and AP kinetics that promote increased excitability in inhibitory neurons (**Figure S1D-E**). Lastly, inhibitory neurons displayed a more depolarized resting membrane potential (RMP) than excitatory neurons (**Figure S1F**).

In summary, this data demonstrate inhibitory and excitatory neurons within the DDH process sensory information in different ways. Inhibitory neurons exhibit more excitable intrinsic properties than their excitatory counterparts, allowing for their preferential recruitment. This preferential recruitment of inhibitory neurons within the mDDH, along with convergence of proprioceptive and cutaneous input to this region, suggests a particularly important role for inhibitory INs within the mDDH in the processing of sensory information during locomotion. We therefore used genetic strategies to target inhibitory mDDH and study their role in motor performance.

Parvalbumin-expressing inhibitory interneurons are confined to the medial deep dorsal horn

The calcium binding protein parvalbumin (PV) is a known marker of inhibitory INs in the brain and spinal cord (Kim et al. 2016; Nahar, Delacroix, and Nam 2021; Boyle et al. 2019). Using the PVTdTomato mouse line, we identified a population of PV-INs confined to the medial portion of the DDH (**Figure 3A**), previously identified as the region receiving convergent sensory input. We named these INs deep dorsal horn parvalbumin-expressing interneurons (dPVs), and found that they represent 18±5.45% of LIV-V. Given PV-INs within LIIi-III of the spinal cord are a mixed excitatory/inhibitory population, we investigated the neurochemical phenotype of dPVs using excitatory and inhibitory markers (**Figure 3B, Figure S2A-D**). We found that dPVs are largely inhibitory, with the majority being purely glycinergic (**Figure S2E-F)**. We also compared the dPV population to two previously characterized inhibitory DDH IN populations defined by the transcription factor Satb2 and the orphan nuclear hormone receptor RORβ. Colocalization analysis showed that dPVs show limited co-expression with Satb2 and RORβ (**Figure S2G-I)**. Therefore, dPVs represent a substantial population of uncharacterized inhibitory INs confined to the mDDH.

To determine whether dPVs are active during locomotion, we again examined c-fos expression following rest, swimming and walking. In line with our previous data showing enhanced activity in inhibitory neurons of the mDDH, we found a significant increase in c-fos expression in dPVs following locomotor activity (**Figure 3C**). dPVs electrophysiological characteristics were similar to those of inhibitory INs within the same region (**Figure 3D-E**). Interestingly, blocking synaptic transmission enhanced sAP frequency, and could alter sAP discharge patterns to promote rhythmic discharge (**Figure S2**J). Therefore, dPVs are active during locomotor activity, and have the intrinsic properties to support spontaneous discharge. Rhythmic inhibition of motoneurons allows for the alternating activity of flexor and extensor muscles during locomotion. Rhythmic output that mimic locomotor activity can be evoked *in vitro* by application of a 'cocktail' containing 5-HT, NMDA, and dopamine. This cocktail depolarized dPVs to increase sAP frequency (**Figure 3F-G**), and in some instances evoked rhythmic discharge (**Figure S2K**). Together, this data shows dPVs are recruited during locomotor activity, and are likely to play an important role as modulators of locomotor output. Given the wide expression of PV throughout the brain, spinal cord, and dorsal root ganglia (DRG), we next sought to devise an experimental approach to specifically target and manipulate the activity of the dPV population.

dPV ablation alters stride frequency

To study the function of dPVs we devised an intersectional genetic approach. First, we found preferential recombination within the DDH when using the PV^{FlpO} mouse-line, avoiding the more dorsal PV-IN population (**Figure S3A**). To restrict expression to the spinal cord, we then examined the co-expression of dPVs with known genetic lineages. As dPVs lie in the dorsoventral interface, we chose to focus on Islet1, and Lbx1 that give rise to dorsal lineages and Sim1, the genetic origin of the ventral V3 population (Gross, Dottori, and Goulding 2002, 1; Lu, Niu, and Alaynick 2015). As dPVs are almost exclusively derived from the Lbx1-lineage (**Figure S2L-N**), we generated an $Lbx1^{Cre}$;PV^{FlpO} intersectional approach to target dPVs throughout the rostrocaudal axis of the spinal cord (**Figure 4A, Figure S3B**), while avoiding recombination within the more superficial dorsal horn, ventral horn, and DRG (**Figure S4A-C**).

The brain was largely devoid of neuronal expression (**Figure S4D**), however, recombination was observed in the cerebellum and brainstem (**Figure S4E-G**). To specifically ablate the dPV population we utilized an intersection of *PV*^{FlpO};Lbx1^{Cre};Tau$^{LSL\text{-}FSF\text{-}DTR}$ with intrathecal injection (I.T.) of Diphtheria toxin (DTx), prepared in a hyperbaric solution to generate mice with ablated dPVs (dPV^{abl}) non-manipulated dPVs (dPV^{norm}) (**Figure 4B-C, Figure S4B-C**) .

After developing an approach to specifically target dPVs, control (dPV^{norm}) and dPV ablated (dPV^{abl}) mice were run on a treadmill at different speeds. A high-speed camera located underneath the transparent belt was used to record paw placement and calculate basic locomotion parameters (**Figure S5A- top diagram**). dPV ablation caused an increase in stride frequency, and decrease in swing time, without major changes to stance (**Figure 4D-E**). To increase stride frequency, animals shorten their stance time with minimal changes to swing (Goslow Jr., Reinking, and Stuart 1973; Halbertsma 1983). We therefore hypothesize that dPVs primary role is to modulate step timing, with changes to swing time a secondary effect. In line with this hypothesis we observed a change in the phase of the transition from stance to swing, with dPV^{abl} mice transitioning later in the step cycle (**Figure 4F**). Given dPVs location within the DDH, a region receiving cutaneous input, we also tested their involvement in corrective motor reflexes. dPV^{abl} and dPV^{norm} mice were walked on a beam with different shapes and sizes (**Figure S5A-C**), a ladder with changing rung patterns (**Figure S5D-G**), and a rotarod (**Figure S5H-I).** Surprisingly, dPV^{abl} mice showed a tendency for fewer slips and a shorter time to cross the beam faster. We found no significant difference between dPV^{abl} and dPV^{norm} horizontal ladder walk (regular or irregular rung pattern) or rotarod (**Figure S5E-I**). Similar to balance beam walk, dPV^{abl} tended to fall at higher speeds, compared to dPV^{norm} (**Figure S5I**). In line with this, dPV^{abl} were able to reach higher speeds on the treadmill than dPV^{norm} mice (**Figure S5J**) Taken together, these data suggest dPVs play an important role in regulating stride frequency by modulating the timing of stance to swing transitions, but do not influence corrective motor reflexes.

dPVs ablation alters joint kinematics at the transition from stance to swing

To determine changes to mice pose underlie the altered locomotor parameters, we next examined mouse kinematics. To do so, mice were walked on the treadmill at 20 cm/s, a speed in which we did not detect a change in stride frequency, which would in-turn lead to stride compensation and alter kinematics. Using DeepLabCut, we tracked hindlimb pose and calculated joint angles throughout the step cycle. We noticed the most profound differences in joint angles were seen at the transition from stance to swing (**Figure 4G-H**). Therefore, we compared joint angles at the posterior extreme position (PEP), occurring at the transition of stance to swing. As a reference, we also compared joint angles at the anterior extreme position (AEP). We found that while there were no significant changes in joint angles during AEP, dPV^{abl} mice showed a decrease in ankle and knee PEP angles, and increase in MTP PEP angle. Altered limb kinematics at lower speeds, where stride frequency was unaffected, suggests dPVs play an important role in priming limb muscles for step cycle transitions - from stance to swing. Further, changes in limb kinematics specific to PEP indicate that dPVs role in locomotion is

phase dependent. We next sought to dissect dPVs circuit connectivity that underlies their role in the behaving animal.

dPVs integrate proprioceptive and cutaneous inputs

dPVs location in the mDDH and role in locomotion suggest they integrate proprioceptive and cutaneous inputs, in particular from the paw. To directly address this, we injected the paw with the anterograde tracer CTB (1%, unconjugated, 7ul) and found that paw primary sensory afferents terminate onto dPVs where they form direct contacts (**Figure S6A**). To assess the contribution of proprioception and cutaneous to dPVs' sensory input, we utilized our genetic strategy to label both modalities. High resolution imaging revealed that both proprioceptive and cutaneous terminals contact dPVs (**Figure 5A**), with significantly more cutaneous input onto dPVs dendrites (**Figure 5B, Figure S6B**).

dPVs distribution suggests they receive input from low threshold and not high- threshold mechanoreceptors (LTMRs vs HTMRs), processing information on innocuous touch. Moreover, innervation from the glabrous skin of the paw suggest more innervation from Aß-LTMRs as opposed to the hairy skin innervating C- and A - LTMRs (Abraira et al. 2017). Using specific genetic crosses to target different LTMRs, we generated a map showing termination pattern of each fiber in respect to the location of dPVs (**Figure S6C**). We found that Aß- field and Aß-Rapidly adapting (Aß-RA) reach dPVs laminas, and are thus likely to directly contact them, which we validated with high resolution confocal imaging (**Figure 5C-D**).

To both validate inputs' functionality and reveal possible polysynaptic connections, we next performed slice electrophysiology where dPVs activity was recorded in response to optogenetic stimulation of sensory afferents (**Figure 5E**). Consistent with our histology results, we found that most monosynaptic input to dPVs originates from proprioceptors, Aß-RA, and Aß- field (**Figure 5F-I**). Additionally, we found that dPVs receive polysynaptic input (distinguished by response jitter and latency, **Figure S6D**) from proprioceptors Aß-, C- and A - LTMR (**Figure 5J-K**). These polysynaptic inputs are likely to be mediated to dPVs by local excitatory INs located in the LTMR- recipient zone (LTMR-RZ), heavily innervated by LTMRs. The CCK lineage is one such population, targeting 27% of LTMR-RZ INs (Abraira et al. 2017). Indeed, using both histology (**Figure S6E**) and electrophysiology (**Figure 5L**), we found that CCK INs functioanlly innervate dPVs. Although activation of LTMRs evoked an excitatory response in dPVs (monosynaptic/polysynaptic), we observed inhibitory currents following the stimulation of proprioceptors and Aß- LTMR (**Figure 5M-N**). These inhibitory currents can be in part mediated by the RorB lineage residing in LTMR-RZ, which targets 18% of LTMR-RZ interneurons (**Figure 3O**).

Taken together, dPVs input connections support integration of proprioceptive and cutaneous inputs from the paw through direct and indirect pathways. We next teased out some of dPVs output targets that support their role in sensorimotor processing.

dPVs form a diffuse inhibitory circuit with spinal cord motor networks

What are dPVs output targets that support their role in motor action? To address this question, we visualized dPVs axon terminals using the intersection *PV*^{FlpO};Lbx1^{Cre};*Rosa*$^{LSL\text{-}FSF\text{-}SynGFP}$ (**Figure 6A- left**). Although our intersection targets the reticular formation, the majority of axon terminals are likely to originate from dPVs and not from the glutamatergic reticulospinal tract (Brownstone and Chopek 2018).

We then used our intersection to generate a map depicting the distribution of dPVs axon terminals across laminas (**Figure 6A- right**). Our map shows a diffuse pattern of dPVs axon terminals through the deep dorsal and ventral horn laminas, suggesting output divergence. We next used immunohistochemistry tools to dissect some of dPVs' targets (**Figure 6B**). The intersection *PV*^{FlpO};Lbx1^{Cre};*Rosa*$^{LSL\text{-}FSF\text{-}synGFP}$/*Rosa*$^{LSL\text{-}FSF\text{-}Tomato}$ revealed that dVPs contact dPVs somas and dendrites, indicating that dPVs form mutual connections (**Figure 6B- upper left**). dPVs terminals reach laminas 7 and 10 where pre-motor neurons such as Renshaw cell and V0c are located. Immunostaining for calbindin (renshaw), and ChAT+ (V0c) neurons, demonstrated direct connections (**Figure 6B- upper right, bottom left**). Further, we show that in lamina 9, dPVs directly contact ChAT positive motor neurons (MN), establishing that dPVs are pre-motor INs (**Figure 6B- bottom right**).

Our behavioral experiment showed that dPVs ablation results in hyperflexion of some joints and hyperextension of others. This suggests that dPVs modulate flexor and extensor motor neurons. Moreover, Lbx1 derived flexor and extensor MNs- innervating premotor INs were shown to be segregated by their neurogenesis day; the first -early (E10.5) and later -late (E12.5) born (Tripodi, Stepien, and Arber 2011). To reveal their neurogenesis, PV^{TdTomato} pregnant moms were injected with the Thymidine analog Edu (50 mg/kg) at E10.5, E11.5 and E12.5, and pups were perfused at P30-P37. Quantification of PV+Edu+ suggests the dPVs innervate both flexors and extensors with a bias toward extensor MNs (**Figure S7A-C)**. To directly test this, *PV*^{FlpO};Lbx1^{Cre};*Rosa*$^{LSL\text{-}FSF\text{-}SynGFP}$ mice were injected with the retrograde tracer CTb555 into chosen knee flexor and extensors (Biceps Femoris/BFP and Vastus lateralis/VL), and ankle flexor and extensors (Tibialis Anterior/TA and Gastrocnemius/Gs, **Figure 6C**). Synaptic analysis revealed that dPVs preferentially target extensor MNs (**Figure 6D)**

Next, we performed slice electrophysiology and recorded from target neurons while optically stimulating dPVs. Recordings were performed from dPVs (*PV*^{FlpO};Lbx1^{Cre};*Rosa*$^{LSL\text{-}FSF\text{-}CatCh(Ai80)}$;PV^{TdTomato}), V0c, lateral MNs, medial MNs, and foot MNs (*PV*^{FlpO};Lbx1^{Cre};*Rosa*$^{LSL\text{-}FSF\text{-}CatCh(Ai80)}$;ChAT^{eGFP}). While all recorded targets responded to photostimulation of dPV terminals, dPVs responded with the highest amplitude and incidence (**Figure 6E-G**). As expected from our histology results, these responses were mediated predominantly by Glycine as shown following application of strychnine (GlyT2 channel blocker), and bicuculline (GABA-A channel blocker, Figure **6H-I**).

Taken together, dPVs integrate proprioceptive and cutaneous inputs and innervate MNs and pre-motor INs in the deep and ventral horn. To directly test if dPVs form a sensorimotor circuit,

we next performed electromyogram activity from flexor and extensor muscles in response to stimulation of sensory nerves.

dPVs mediate cutaneous- evoked muscle inhibition

To perform sensorimotor processing for locomotion, dPVs must relay sensory inputs to motor networks where their activity will affect motor response. We thus proceeded by studying the role of dPVs in muscle response evoked by the activation of paw cutaneous inputs. dPVs^{abl} and dPVs^{norm} were implanted with nerve cuffs on 2 cutaneous nerves: the right sural and left saphenous nerves, innervating the ventral and dorsal paw. Electromyogram (EMG) electrodes were implanted in the right and left semitendinosus (St, knee flexor), right vastus lateralis (VL, knee extensor), right and left gastrocnemius (Gs, ankle extensor), and left tibialis anterior (ankle flexor). Following the stimulation of each nerve, activity was recorded in both ipsi and contralateral muscle (**Figure 7A**). Latency to response decreased in the knee flexor St, and ankle flexor TA ipsilateral to the saphenous nerve, and in the ankle extensor Gs, ipsilateral to the sural and contralateral to the saphenous nerves (**Figure 7A-C, Figure S8A-C**).

These faster responses in dPVs^{abl} suggest a loss of inhibition following dPVs ablation. To directly test this, we designed a 2- nerve assay paradigm (**Figure 7D- top**) in which local cutaneous inputs will suppress a motor response if inhibitory pathways are present. Nerve cuffs and EMG electrodes were implanted as described above. A chosen nerve was stimulated (**Figure 7D-bottom**, black lighting). 20 EMG responses were averaged to calculate the expected response to stimulation of the chosen nerve. Following, stimulation of the second nerve (yellow lightning) was paired to the first, at various delays. Different delays were used to account for differences in muscle response latency to each nerve, which can be different within mice and muscles. Each response was then compared to the expected response, aligned to the beginning of the first stimulation (**Figure 7D**). For each muscle, a single delay was chosen for further analysis as explained in methods. 10-15 ms following the stimulation of the second nerve, if response to the 2- nerve stimulation was lower than the expected response, we concluded that the trial includes an inhibition component (**Figure 7E**). Experimental setup allowed us to explore the participation of dPVs in both local inhibition (when the second nerve stimulated is ipsilateral to the recorded muscle) and contralateral inhibition (when the second nerve stimulated is contralateral to the recorded muscle). Quantifying percent inhibition (the percentage of trials in which inhibition was detected), dPVs^{abl} showed a loss of ipsilateral inhibition from the saphenous nerve to the knee flexor St, and from the sural nerve to the ankle extensor Gs (**Figure 7F**). Additionally, dPVs^{abl} showed a loss of contralateral inhibition from the sural nerve to the ankle flexor TA (**Figure S8D-F**)

In conclusion, here we characterize the role of the DDH in multimodal integration of proprioceptive and cutaneous inputs for locomotion. We find that DDH inhibitory interneurons are highly responsive to sensory inputs, and as such are particularly recruited in locomotion that involves integration of proprioceptive and cutaneous inputs. We proceed by identifying a novel DDH PV expressing glycinergic interneurons (dPVs), shown to increase their excitability in locomotion conditions. Using genetic tools to specifically ablate dPVs, we reveal that dPVs

modulate locomotion in a speed and phase dependent manner, suggesting that dPVs are involved in dynamic sensorimotor interaction. Indeed, by characterizing their connectivity we find that dPVs integrate proprioceptive and cutaneous input to inhibit DDH and ventral horn neurons, including pre-motor and motor neurons. Lastly, we directly demonstrate a loss of sensory evoked muscle inhibition following the ablation of dPVs.

DISCUSSION

The circuits that mediate cutaneous modulation of locomotion are largely unknown. Our simplified model using dPVs demonstrates that cutaneous and proprioceptive inputs converge on inhibitory INs located in the DDH, information that is then relayed to spinal cord motor networks to modulate the step cycle. We suggest that cutaneous and proprioceptive convergence is not functionally redundant. Instead, convergence is necessary for the emergence of more complex processing as well as divergent influence at the network level, thereby increasing the diversity of mechanisms by which sensory information can influence network activity for the purpose of movement execution and refinement. Moreover, we propose two ways by which DDH INs mediate dynamic sensory modulation of motor networks, i.e.,that is state and phase dependent. First, by integrating inputs from multiple sources (cutaneous, proprioceptive, CPGs) the output of DDH INs is highly regulated, thereby incoming inputs are only relayed under certain circumstances. Second, excitatory and inhibitory tonic firing DDH INs might work in tandem to maintain the excitation- inhibition balance of spinal cord motor networks. We propose that by maintaining this balance, the DDH modulates the gain of motor networks, thereby changing the responsiveness to incoming sensory input.

Convergence of proprioceptive and cutaneous input by deep dorsal horn interneurons for the modulation of locomotion

With the growing development of molecular and genetic tools, studies are rushing to tease out the distinct functions of neuronal subsets. However, it is important to recognize, as shown by a recent study (Gatto et al. 2021), that the spinal cord dorsal horn displays a laminar organization, where molecularly heterogeneous INs show overlapping roles. In a similar fashion, the DDH, suggested to integrate proprioceptive and cutaneous inputs (Moschovakis, Solodkin, and Burke 1992; Orlovskiĭ and Fel'dman 1972; A. G. Brown and Fyffe 1981; Edgley and Jankowska 1987; Hongo et al. 1989; Abraira et al. 2017) and shown to harbor premotor INs (Moschovakis, Solodkin, and Burke 1992; Levine et al. 2014) is thought to play a significant role in sensorimotor processing. Here we use new genetic tools and show that indeed, the medial portion of laminas 4-5 of the DDH integrates multimodal proprioceptive and cutaneous inputs. We focus our attention on dPV interneurons, representing a large portion of laminas 4-5, and by functionally characterizing their input-output connectivity, we provide evidence for a role of the DDH interneuron in sensorimotor processes.

Other studies have probed the role of DDH INs in sensorimotor processing using genetic tools. The inhibitory Satb2 INs were shown to relay nociceptive and proprioceptive information to

motor circuits, and appropriately, participate in both pain withdrawal and locomotion (Hilde et al. 2016). Also participating in locomotion, RorB INs were shown to gate incoming proprioceptive input by presynaptic inhibition (Koch et al. 2017). Excitatory dI3 INs modulate grasping by transmitting innocuous cutaneous input to motor circuits (Bui et al. 2013). While other dorsal horn populations have been characterized, this paper provides characterization of a novel, previously uncharacterized population, and adds to the growing body of knowledge of the role of the DDH. Further, although their existence has been assumed from studies demonstrating a role for cutaneous input in the modulation of motor output, dPVs are the first genetically identified inhibitory INs shown to form a spinal cord cutaneous- motor circuit.

The existence of spinal cord INs that integrate multimodal sensory input and modulate locomotion, raise the question of why such convergence is important for locomotion?
By comparison to other sensory systems, such as the visual system, neurons' visual receptive field becomes more complex at successive stages of the visual pathway. These more complex receptive fields are thought to result from convergence of inputs from a number of "simple" cells, having a more simple receptive field (Martinez and Alonso 2003; Ringach 2004). This example makes one realize that convergence is a necessary mechanism for more complex processing to occur. In the case of locomotion, the complexity is manifested by incoming sensory input from various sensory modalities. For the next step to be modulated accurately in response to the sensory environment, integration of multimodal information is necessary.

This paper and others identify INs that integrate multimodal sensory input(Hilde et al. 2016; Koch et al. 2017; Bui et al. 2013). Why is it beneficial that such convergence occurs on INs as opposed to the output neurons, in this case, the motor neuron? In the case of cutaneous and proprioceptive inputs, direct inputs can only be integrated on INs as cutaneous inputs do not reach lamina 9, where motor neurons are located. We do not exclude the possibility that MNs integrate indirect cutaneous and proprioceptive information. However, we propose two reasons why such "early" convergence is beneficial for motor performance. First, it reduces the amount of processing required to be performed by motor neurons. As the last order neuron in the motor pathway, motor neurons must take multiple information into consideration. Early processing can thus reduce the load on motor neurons. Second, locomotion requires the coordination of muscles across all limb's joints and between all limbs. Thus, incoming sensory input must modulate the activity of several muscles in parallel. Sensory input convergence on INs as opposed to motor neurons offers the opportunity for output convergence to multiple motor and pre-motor neurons that can modulate the activity of several muscles in parallel.

Dynamic modulation of locomotion by sensory inputs

In this study we identify the DDH parvalbumin expressing INs (dPVs) that functionally integrate direct multimodal sensory inputs from proprioceptors and Aß-LTMRs as well as indirect input from A - LTMR, C- LTMRs and local excitatory interneurons. Ablation of dPVs results in a state, speed and phase dependent phenotype. Mice walked normally on a horizontal ladder, balance beam with different sizes and rotarod. However, detailed analysis of high speed videos of treadmill walking revealed changes to locomotion that were more pronounced at high speeds.

At high speeds- swing duration was shorter, and stride frequency increased. Although there was no change in phase durations at low speeds, tracking of hindlimb pose showed reduced knee and ankle joint angles during late stance, resulting in hyperflexion of the ankle and knee.

Our results are consistent with prior observations indicating that under normal conditions, sensory input is not required for the basic expression of locomotion. Early experiments by Sherrington and others showed that denervation of hindlimb cutaneous input, proprioceptive input, or both, did not prevent locomotion. Thus, it is reasonable that the ablation of a spinal interneuron that selectively integrates subtypes of proprioceptive and cutaneous input would not have a major effect on basic locomotion. Nonetheless, when locomotion was tested in challenging conditions, removal of sensory afferents revealed changes to locomotion. For example, soon after complete or incomplete removal of hindpaw cutaneous afferents in cats, studies reported impairments in ladder walk (Bouyer and Rossignol 1998), crossing of narrow beam (Goldberger 1977) and high speed treadmill walk (Wetzel et al. 1976). Similarly, we found that ablation of dPVs results in a state- and speed- dependent phenotype, where impaired locomotion was observed in high speed treadmill walk but not in other tasks. This suggests that lumbosacral dPVs, ablated in this paper, process sensory input important for high speed treadmill walk, but not ladder or beam. What type of sensory input do dPVs integrate that account for this phenotype? A study (Akay et al. 2014) showed that mice lacking proprioceptive input from muscle spindles display reduced precision in foot placement on a horizontal ladder, suggesting that dPVs integrate less Ia/II afferents than GTOs.

Mice increase their walking speed by decreasing stance duration, with minimal change to swing duration. Regulation of extensor activity during stance was shown to be mediated by Ib - GTO afferens in cats (J. Maxwell Donelan and Pearson 2004; J. M. Donelan and Pearson 2004; J. M. Donelan, McVea, and Pearson 2009). However, experiments in both mice and humans suggest that Ia afferents also participate in the regulation speed-dependent amplitude of muscle activity. Recently developed mouse genetic tools distinguish Ia/II and Ib proprioceptive afferents (Wu et al. 2021). While out of the scope of the current paper, more experiments utilizing these tools will enable us to decipher the relative contribution of different proprioceptive subtypes to dPVs input.

Although less studied, cutaneous mechanoreceptors of the footpad can also play a similar role to Ib afferents in load detection and play a role in the modulation of stance duration and speed (Duysens, Clarac, and Cruse 2000). Additionally, dPVs role in high speed locomotion might be due to integration of supraspinal inputs. dPVs might integrate supraspinal input important for speed regulation. For example, a study (Caggiano et al. 2018) found that the cuneiform (CnF) and the pedunculopontine (PPN) nuclei located in the mesencephalic locomotor region control speed selection. Activation of both nuclei was enough to elicit locomotion, while CnF elicited slow exploratory locomotion and PPN was able to induce a range of locomotion speed, depending on stimulation frequency. Nuclei of the reticular formation such as medullary reticular formation (MRF), gigantocellular nucleus (Gi) and the reticular magnocellular nucleus (Mc), are thought to mediate the final locomotor command from MLR (Brownstone and Chopek 2018; Dubuc et al. 2008; Garcia-Rill, Skinner, and Fitzgerald 1985; McClellan and Grillner 1984; Mori 1987; Takakusaki et al. 2003). Specifically, the lateral paragigantocellular nucleus (LPGi) was

demonstrated as an important functional reticulospinal locomotor command node regulating the expression of high-speed locomotion (Caggiano et al. 2018; Capelli et al. 2017). Thus, a combination of descending inputs from MLR and the reticular formation might be a mechanism by which dPVs are recruited during high speed but not low speed locomotion.

Further, ablation of dPVs resulted in a phase dependent phenotype. Analysis of joint angles showed hyper-flexion of the ankle and knee only during late stance. Analysis of paw placement showed a shorter swing, but minimal change to stance duration. This phase- dependency is consistent with other studies showing different roles of sensory inputs during the different phases of locomotion. For example, similar to our results, Bouyer and Rossignol showed that removal of hindpaw cutaneous afferents, in otherwise intact cats, results in faster swing, but no change in stance duration (Bouyer and Rossignol 1998). Anderrson and Grillner showed in curarized spinal cats, that activation of hip proprioceptors can shorten or prolong specific subphases of the locomotor cycle, depending on the time the movement was applied (Andersson and Grillner 1983). Experiments where cutaneous or proprioceptive reflexes were entrained during locomotion showed interesting results suggesting dynamic modulation of reflex response depending on the locomotion phase. For example, electrical or mechanical stimulation of the dorsum of the foot during swing of forward locomotion, produces a similar pattern of muscle activation involving activation of knee flexors, as well as ankle and hip extensors to move the leg away from and over the obstacle (Forssberg 1979; Schillings, Van Wezel, and Duysens 1996; Forssberg, Grillner, and Rossignol 1975; 1977). On the other hand, stimulation during stance does not recruit flexors, but instead results in a short latency amplitude increase of already active ankle and knee extensor muscles (Forssberg, Grillner, and Rossignol 1975). Reflex reversal was also shown when the stretch reflex was activated during walking. For example, when ankle stretch is induced during stance, response amplitude is doubled, relative to when it is induced during swing. However, because of the long response, Ia afferents, innervating muscle spindles are thought to contribute very little to locomotion, under normal conditions. On the other hand, Ib afferents innervating GTOs, were shown to discharge maximally during stance, and their discharge rate is closely linked to the force output. Since Ia are thought to have little contribution, the role of proprioceptors in locomotion is attributed to Ib. Additionally, while in this paper we put focus on the role of low threshold mechanoreceptors in locomotion, a phase dependent role for nociceptors was also demonstrated in locomotion. dPVs location in the DDH is suggestive of integration of low threshold LTMRs however HTMRs such as the cGRP positive afferents can innervate dPVs and participate in their role in modulation of locomotion.

Together, dPVs dynamic role in the modulation of locomotion is consistent with previous literature of the role of sensory afferents in locomotion.while further experiment are needed to better understand the mechanism for this dynamic modulation, our results show that dPVs firing rate has a wide dynamic range in response to current injections, suggesting their activity can be up and down regulated as necessary. Further, we found that application of NA+DA cocktail, previously used to induce fictive locomotion, can modulate dPVs membrane potential, suggesting that CPGs can modulate dPVs membrane potential in a phase and state dependent manner.

The role of inhibition in the spinal cord

We found that inhibitory INs located in the medial DDH are preferentially recruited during weight bearing locomotion, requiring the integration of cutaneous and proprioceptive inputs. The role of inhibition has been extensively studied, in both the brain and spinal cord. Studies show that experimentally disrupting excitation- inhibition balance leads to aberrant neural states (Dudek and Sutula 2007). Further, it was demonstrated in various brain sensory systems, that a change in the excitatory drive leads to a concomitant change in the inhibitory drive to maintain the balance (Anderson et al. 2000; Poo and Isaacson 2009; Wehr and Zador 2003; Wilent and Contreras 2005; Z. Li et al. 2003). Evidence for this balance was also demonstrated in the spinal cord. In turtles, recordings from motor neurons during scratching revealed that changes in neuronal conductance were accompanied by a simultaneous increase in rhythmic inhibition and excitation (Berg, Alaburda, and Hounsgaard 2007; Petersen et al. 2014). This simultaneous inhibition and excitation has been termed “push-pull”, and is thought to be a mechanism for gain control, i.e. to induce a divisive change in the input-output relationship of neurons (Johnson et al. 2012). This was demonstrated in ankle extensor motor neurons of the feline where inhibitory and excitatory inputs from flexor and extensor Ia proprioceptive afferents, respectively, behaved in a push-pull manner and provided tonic inhibition and excitation to motor neurons. As a result of these background “noise”, response gain to phasic sensory input from the same afferents was increased. Here we identify dPVs that relay cutaneous information to motor neurons. While dPVs show phasic response to proprioceptive and cutaneous input, they are also tonically active. Additionally, we show that excitatory INs in the DDH similarly integrate cutaneous and proprioceptive input and are mostly tonically active. Thus dPVs might act in tandem to an excitatory component that receives the same inputs and excites the same motor neurons to maintain their inhibition- excitation balance in order to “sharpen” motor neuron response to the sensory input. Additionally, decreasing dPVs firing frequency by modulation of CPGs or neuromodulators can be used to decrease the motor neurons gain so it is less sensitive to incoming sensory input, which can explain dPVs state, speed and phase dynamic role.
In the superficial dorsal horn, while inhibitory neurons are mostly tonically active, excitatory interneurons' firing properties are more heterogeneous. Here we find that in the DDH, most inhibitory and excitatory neurons are tonic firing. Combined with studies demonstrating the DDH contains the largest pool of pre-motor neurons, one role of the DDH might be in gain modulation of motor neurons.

REFERENCES

Abraira, Victoria E., Emily D. Kuehn, Anda M. Chirila, Mark W. Springel, Alexis A. Toliver, Amanda L. Zimmerman, Lauren L. Orefice, et al. 2017. “The Cellular and Synaptic Architecture of the Mechanosensory Dorsal Horn.” *Cell* 168 (1–2): 295-310.e19. https://doi.org/10.1016/j.cell.2016.12.010.

Acton, David, Xiangyu Ren, Stefania Di Costanzo, Antoine Dalet, Steeve Bourane, Ilaria Bertocchi, Carola Eva, and Martyn Goulding. 2019. “Spinal Neuropeptide Y1 Receptor-Expressing Neurons Form an Essential Excitatory Pathway for Mechanical

Itch." *Cell Reports* 28 (3): 625-639.e6. https://doi.org/10.1016/j.celrep.2019.06.033.
Akay, Turgay, Hernish J. Acharya, Karim Fouad, and Keir G. Pearson. 2006. "Behavioral and Electromyographic Characterization of Mice Lacking EphA4 Receptors." *Journal of Neurophysiology* 96 (2): 642–51. https://doi.org/10.1152/jn.00174.2006.
Akay, Turgay, Warren G. Tourtellotte, Silvia Arber, and Thomas M. Jessell. 2014. "Degradation of Mouse Locomotor Pattern in the Absence of Proprioceptive Sensory Feedback." *Proceedings of the National Academy of Sciences of the United States of America* 111 (47): 16877–82. https://doi.org/10.1073/pnas.1419045111.
Albisetti, Gioele W., Martina Pagani, Evgenia Platonova, Ladina Hösli, Helge C. Johannssen, Jean-Marc Fritschy, Hendrik Wildner, and Hanns Ulrich Zeilhofer. 2019. "Dorsal Horn Gastrin-Releasing Peptide Expressing Neurons Transmit Spinal Itch But Not Pain Signals." *The Journal of Neuroscience: The Official Journal of the Society for Neuroscience* 39 (12): 2238–50. https://doi.org/10.1523/JNEUROSCI.2559-18.2019.
Anderson, J., I. Lampl, I. Reichova, M. Carandini, and D. Ferster. 2000. "Stimulus Dependence of Two-State Fluctuations of Membrane Potential in Cat Visual Cortex." *Nature Neuroscience* 3 (6): 617–21. https://doi.org/10.1038/75797.
Andersson, O., and S. Grillner. 1983. "Peripheral Control of the Cat's Step Cycle. II. Entrainment of the Central Pattern Generators for Locomotion by Sinusoidal Hip Movements during 'Fictive Locomotion.'" *Acta Physiologica Scandinavica* 118 (3): 229–39. https://doi.org/10.1111/j.1748-1716.1983.tb07267.x.
Aristotle's De Motu Animalium. 1986. https://press.princeton.edu/books/paperback/9780691020358/aristotles-de-motu-animalium.
Berg, Rune W., Aidas Alaburda, and Jørn Hounsgaard. 2007. "Balanced Inhibition and Excitation Drive Spike Activity in Spinal Half-Centers." *Science (New York, N.Y.)* 315 (5810): 390–93. https://doi.org/10.1126/science.1134960.
Bouyer, L. J., and S. Rossignol. 1998. "The Contribution of Cutaneous Inputs to Locomotion in the Intact and the Spinal Cat." *Annals of the New York Academy of Sciences* 860 (November): 508–12. https://doi.org/10.1111/j.1749-6632.1998.tb09090.x.
Boyle, Kieran A., Mark A. Gradwell, Toshiharu Yasaka, Allen C. Dickie, Erika Polgár, Robert P. Ganley, Desmond P. H. Orr, et al. 2019. "Defining a Spinal Microcircuit That Gates Myelinated Afferent Input: Implications for Tactile Allodynia." *Cell Reports* 28 (2): 526-540.e6. https://doi.org/10.1016/j.celrep.2019.06.040.
Brown, A G, and R E Fyffe. 1981. "Direct Observations on the Contacts Made between Ia Afferent Fibres and Alpha-Motoneurones in the Cat's Lumbosacral Spinal Cord." *The Journal of Physiology* 313: 121–40.
Brown, Thomas Graham, and Charles Scott Sherrington. 1911. "The Intrinsic Factors in the Act of Progression in the Mammal." *Proceedings of the Royal Society of London. Series B, Containing Papers of a Biological Character* 84 (572): 308–19. https://doi.org/10.1098/rspb.1911.0077.
Browne, Tyler J., Mark A. Gradwell, Jacqueline A. Iredale, Jessica F. Maden, Robert J. Callister, David I. Hughes, Christopher V. Dayas, and Brett A. Graham. 2020. "Transgenic Cross-Referencing of Inhibitory and Excitatory Interneuron Populations to Dissect Neuronal Heterogeneity in the Dorsal Horn." *Frontiers in Molecular Neuroscience* 13: 32.

https://doi.org/10.3389/fnmol.2020.00032.
Brownstone, Robert M., and Jeremy W. Chopek. 2018. “Reticulospinal Systems for Tuning Motor Commands.” *Frontiers in Neural Circuits* 12: 30. https://doi.org/10.3389/fncir.2018.00030.
Bui, Tuan V., Turgay Akay, Osama Loubani, Thomas S. Hnasko, Thomas M. Jessell, and Robert M. Brownstone. 2013. “Circuits for Grasping: Spinal DI3 Interneurons Mediate Cutaneous Control of Motor Behavior.” *Neuron* 78 (1): 191–204. https://doi.org/10.1016/j.neuron.2013.02.007.
Caggiano, V, R Leiras, H Goñi-Erro, D Masini, C Bellardita, J Bouvier, V Caldeira, G Fisone, and O Kiehn. 2018. “Midbrain Circuits That Set Locomotor Speed and Gait Selection.” *Nature* 553 (7689): 455–60. https://doi.org/10.1038/nature25448.
Capelli, Paolo, Chiara Pivetta, Maria Soledad Esposito, and Silvia Arber. 2017. “Locomotor Speed Control Circuits in the Caudal Brainstem.” *Nature* 551 (7680): 373–77. https://doi.org/10.1038/nature24064.
Donelan, J. M., D. A. McVea, and K. G. Pearson. 2009. “Force Regulation of Ankle Extensor Muscle Activity in Freely Walking Cats.” *Journal of Neurophysiology* 101 (1): 360–71. https://doi.org/10.1152/jn.90918.2008.
Donelan, J. M., and K. G. Pearson. 2004. “Contribution of Force Feedback to Ankle Extensor Activity in Decerebrate Walking Cats.” *Journal of Neurophysiology* 92 (4): 2093–2104. https://doi.org/10.1152/jn.00325.2004.
Donelan, J. Maxwell, and Keir G. Pearson. 2004. “Contribution of Sensory Feedback to Ongoing Ankle Extensor Activity during the Stance Phase of Walking.” *Canadian Journal of Physiology and Pharmacology* 82 (8–9): 589–98. https://doi.org/10.1139/y04-043.
Dubuc, Réjean, Frédéric Brocard, Myriam Antri, Karine Fénelon, Jean-François Gariépy, Roy Smetana, Ariane Ménard, et al. 2008. “Initiation of Locomotion in Lampreys.” *Brain Research Reviews* 57 (1): 172–82. https://doi.org/10.1016/j.brainresrev.2007.07.016.
Dudek, F. Edward, and Thomas P. Sutula. 2007. “Epileptogenesis in the Dentate Gyrus: A Critical Perspective.” *Progress in Brain Research* 163: 755–73. https://doi.org/10.1016/S0079-6123(07)63041-6.
Duysens, J., F. Clarac, and H. Cruse. 2000. “Load-Regulating Mechanisms in Gait and Posture: Comparative Aspects.” *Physiological Reviews* 80 (1): 83–133. https://doi.org/10.1152/physrev.2000.80.1.83.
Edgley, S. A., and E. Jankowska. 1987. “Field Potentials Generated by Group II Muscle Afferents in the Middle Lumbar Segments of the Cat Spinal Cord.” *The Journal of Physiology* 385 (April): 393–413. https://doi.org/10.1113/jphysiol.1987.sp016498.
Forssberg, H. 1979. “Stumbling Corrective Reaction: A Phase-Dependent Compensatory Reaction during Locomotion.” *Journal of Neurophysiology* 42 (4): 936–53. https://doi.org/10.1152/jn.1979.42.4.936.
Forssberg, H., S. Grillner, and S. Rossignol. 1975. “Phase Dependent Reflex Reversal during Walking in Chronic Spinal Cats.” *Brain Research* 85 (1): 103–7. https://doi.org/10.1016/0006-8993(75)91013-6.
Forssberg, H., S. Grillner, and S. Rossignol. 1977. “Phasic Gain Control of Reflexes from the Dorsum of the Paw during Spinal Locomotion.” *Brain Research* 132 (1): 121–39. https://doi.org/10.1016/0006-8993(77)90710-7.

Garcia-Rill, E., R. D. Skinner, and J. A. Fitzgerald. 1985. “Chemical Activation of the Mesencephalic Locomotor Region.” *Brain Research* 330 (1): 43–54. https://doi.org/10.1016/0006-8993(85)90006-x.

Gatto, Graziana, Steeve Bourane, Xiangyu Ren, Stefania Di Costanzo, Peter K. Fenton, Priyabrata Halder, Rebecca P. Seal, and Martyn D. Goulding. 2021. “A Functional Topographic Map for Spinal Sensorimotor Reflexes.” *Neuron* 109 (1): 91-104.e5. https://doi.org/10.1016/j.neuron.2020.10.003.

Goldberger, M. E. 1977. “Locomotor Recovery after Unilateral Hindlimb Deafferentation in Cats.” *Brain Research* 123 (1): 59–74. https://doi.org/10.1016/0006-8993(77)90643-6.

Goslow Jr., George E., Robert M. Reinking, and Douglas G. Stuart. 1973. “The Cat Step Cycle: Hind Limb Joint Angles and Muscle Lengths during Unrestrained Locomotion.” *Journal of Morphology* 141 (1): 1–41. https://doi.org/10.1002/jmor.1051410102.

Grillner, S., and S. Rossignol. 1978. “On the Initiation of the Swing Phase of Locomotion in Chronic Spinal Cats.” *Brain Research* 146 (2): 269–77. https://doi.org/10.1016/0006-8993(78)90973-3.

Gross, Michael K., Mirella Dottori, and Martyn Goulding. 2002. “Lbx1 Specifies Somatosensory Association Interneurons in the Dorsal Spinal Cord.” *Neuron* 34 (4): 535–49. https://doi.org/10.1016/S0896-6273(02)00690-6.

Gruner, J. A., and J. Altman. 1980. “Swimming in the Rat: Analysis of Locomotor Performance in Comparison to Stepping.” *Experimental Brain Research* 40 (4): 374–82. https://doi.org/10.1007/BF00236146.

Halbertsma, J. M. 1983. “The Stride Cycle of the Cat: The Modelling of Locomotion by Computerized Analysis of Automatic Recordings.” *Acta Physiologica Scandinavica. Supplementum* 521: 1–75.

Hampton, Thomas G., Melissa R. Stasko, Ajit Kale, Ivo Amende, and Alberto C. S. Costa. 2004. “Gait Dynamics in Trisomic Mice: Quantitative Neurological Traits of Down Syndrome.” *Physiology & Behavior* 82 (2–3): 381–89. https://doi.org/10.1016/j.physbeh.2004.04.006.

Hilde, Kathryn L., Ariel J. Levine, Christopher A. Hinckley, Marito Hayashi, Jessica M. Montgomery, Miriam Gullo, Shawn P. Driscoll, et al. 2016. “Satb2 Is Required for the Development of a Spinal Exteroceptive Microcircuit That Modulates Limb Position.” *Neuron* 91 (4): 763–76. https://doi.org/10.1016/j.neuron.2016.07.014.

Hongo, T., S. Kitazawa, Y. Ohki, and M. Xi. 1989. “Functional Identification of Last-Order Interneurones of Skin Reflex Pathways in the Cat Forelimb Segments.” *Brain Research*, December. https://www.meta.org/papers/functional-identification-of-last-order/2611673.

Hunt, Stephen P., Adrian Pini, and Gerard Evan. 1987. “Induction of C-Fos-like Protein in Spinal Cord Neurons Following Sensory Stimulation.” *Nature* 328 (6131): 632–34. https://doi.org/10.1038/328632a0.

J, Duysens, and Pearson Kg. 1980. “Inhibition of Flexor Burst Generation by Loading Ankle Extensor Muscles in Walking Cats.” *Brain Research* 187 (2). https://doi.org/10.1016/0006-8993(80)90206-1.

Johnson, Michael D., Allison S. Hyngstrom, Marin Manuel, and C. J. Heckman. 2012. “Push-Pull Control of Motor Output.” *The Journal of Neuroscience: The Official Journal of the Society for Neuroscience* 32 (13): 4592–99. https://doi.org/10.1523/JNEUROSCI.4709-11.2012.

Kim, Hoseok, Sofie Ährlund-Richter, Xinming Wang, Karl Deisseroth, and Marie Carlén. 2016. "Prefrontal Parvalbumin Neurons in Control of Attention." *Cell* 164 (1–2): 208–18. https://doi.org/10.1016/j.cell.2015.11.038.

Koch, Stephanie C., Marta Garcia Del Barrio, Antoine Dalet, Graziana Gatto, Thomas Günther, Jingming Zhang, Barbara Seidler, Dieter Saur, Roland Schüle, and Martyn Goulding. 2017. "RORβ Spinal Interneurons Gate Sensory Transmission during Locomotion to Secure a Fluid Walking Gait." *Neuron* 96 (6): 1419-1431.e5. https://doi.org/10.1016/j.neuron.2017.11.011.

Laflamme, Olivier D., and Turgay Akay. 2018. "Excitatory and Inhibitory Crossed Reflex Pathways in Mice." *Journal of Neurophysiology* 120 (6): 2897–2907. https://doi.org/10.1152/jn.00450.2018.

Laflamme, Olivier D., Marwan Ibrahim, and Turgay Akay. 2022. "Crossed Reflex Responses to Flexor Nerve Stimulation in Mice." *Journal of Neurophysiology* 127 (2): 493–503. https://doi.org/10.1152/jn.00385.2021.

Lajoie, Y., N. Teasdale, J. D. Cole, M. Burnett, C. Bard, M. Fleury, R. Forget, J. Paillard, and Y. Lamarre. 1996. "Gait of a Deafferented Subject without Large Myelinated Sensory Fibers below the Neck." *Neurology* 47 (1): 109–15. https://doi.org/10.1212/wnl.47.1.109.

Lehnert, Brendan P., Celine Santiago, Erica L. Huey, Alan J. Emanuel, Sophia Renauld, Nusrat Africawala, Ilayda Alkislar, et al. 2021. "Mechanoreceptor Synapses in the Brainstem Shape the Central Representation of Touch." *Cell* 184 (22): 5608-5621.e18. https://doi.org/10.1016/j.cell.2021.09.023.

Levine, Ariel J., Christopher A. Hinckley, Kathryn L. Hilde, Shawn P. Driscoll, Tiffany H. Poon, Jessica M. Montgomery, and Samuel L. Pfaff. 2014. "Identification of a Cellular Node for Motor Control Pathways." *Nature Neuroscience* 17 (4): 586–93. https://doi.org/10.1038/nn.3675.

Li, Dongxiao, Yundu Li, Yunyun Tian, Zuoshang Xu, and Yansu Guo. 2019. "Direct Intrathecal Injection of Recombinant Adeno-Associated Viruses in Adult Mice." *JoVE (Journal of Visualized Experiments)*, no. 144 (February): e58565. https://doi.org/10.3791/58565.

Li, Zhang, Tan Ay, Schreiner Ce, and Merzenich Mm. 2003. "Topography and Synaptic Shaping of Direction Selectivity in Primary Auditory Cortex." *Nature* 424 (6945). https://doi.org/10.1038/nature01796.

Lu, Daniel C., Tianyi Niu, and William A. Alaynick. 2015. "Molecular and Cellular Development of Spinal Cord Locomotor Circuitry." *Frontiers in Molecular Neuroscience* 8 (June): 25. https://doi.org/10.3389/fnmol.2015.00025.

Luo, Wenqin, Hideki Enomoto, Frank L. Rice, Jeffrey Milbrandt, and David D. Ginty. 2009. "Molecular Identification of Rapidly Adapting Mechanoreceptors and Their Developmental Dependence on Ret Signaling." *Neuron* 64 (6): 841–56. https://doi.org/10.1016/j.neuron.2009.11.003.

Martinez, Luis M., and Jose-Manuel Alonso. 2003. "Complex Receptive Fields in Primary Visual Cortex." *The Neuroscientist: A Review Journal Bringing Neurobiology, Neurology and Psychiatry* 9 (5): 317–31. https://doi.org/10.1177/1073858403252732.

Mathis, Alexander, Pranav Mamidanna, Kevin M. Cury, Taiga Abe, Venkatesh N. Murthy, Mackenzie Weygandt Mathis, and Matthias Bethge. 2018. "DeepLabCut: Markerless Pose Estimation of User-Defined Body Parts with Deep Learning." *Nature Neuroscience*

21 (9): 1281–89. https://doi.org/10.1038/s41593-018-0209-y.
McClellan, A. D., and S. Grillner. 1984. “Activation of ‘fictive Swimming’ by Electrical Microstimulation of Brainstem Locomotor Regions in an in Vitro Preparation of the Lamprey Central Nervous System.” *Brain Research* 300 (2): 357–61. https://doi.org/10.1016/0006-8993(84)90846-1.
Miranda, Camila Oliveira, Krisztina Hegedüs, Hendrik Wildner, Hanns Ulrich Zeilhofer, and Miklós Antal. 2022. “Morphological and Neurochemical Characterization of Glycinergic Neurons in Laminae I-IV of the Mouse Spinal Dorsal Horn.” *The Journal of Comparative Neurology* 530 (3): 607–26. https://doi.org/10.1002/cne.25232.
Morgan, James I., and Tom Curran. 1986. “Role of Ion Flux in the Control of C-Fos Expression.” *Nature* 322 (6079): 552–55. https://doi.org/10.1038/322552a0.
Mori, S. 1987. “Integration of Posture and Locomotion in Acute Decerebrate Cats and in Awake, Freely Moving Cats.” *Progress in Neurobiology* 28 (2): 161–95. https://doi.org/10.1016/0301-0082(87)90010-4.
Moschovakis, A. K., M. Solodkin, and R. E. Burke. 1992. “Anatomical and Physiological Study of Interneurons in an Oligosynaptic Cutaneous Reflex Pathway in the Cat Hindlimb.” *Brain Research* 586 (2): 311–18. https://doi.org/10.1016/0006-8993(92)91641-q.
Muir, G. D., and J. D. Steeves. 1995. “Phasic Cutaneous Input Facilitates Locomotor Recovery after Incomplete Spinal Injury in the Chick.” *Journal of Neurophysiology* 74 (1): 358–68. https://doi.org/10.1152/jn.1995.74.1.358.
Nahar, Lailun, Blake M. Delacroix, and Hyung W. Nam. 2021. “The Role of Parvalbumin Interneurons in Neurotransmitter Balance and Neurological Disease.” *Frontiers in Psychiatry* 12. https://www.frontiersin.org/article/10.3389/fpsyt.2021.679960.
Orlovskiĭ, G. N., and A. G. Fel’dman. 1972. “[Classification of the neurons of the lumbo-sacral region of the spinal cord in accordance with their discharge patterns during provoked locomotion].” *Neirofiziologiia = Neurophysiology* 4 (4): 410–17.
Pearson, K. G., H. Acharya, and K. Fouad. 2005. “A New Electrode Configuration for Recording Electromyographic Activity in Behaving Mice.” *Journal of Neuroscience Methods* 148 (1): 36–42. https://doi.org/10.1016/j.jneumeth.2005.04.006.
Petersen, Peter C., Mikkel Vestergaard, Kristian H. R. Jensen, and Rune W. Berg. 2014. “Premotor Spinal Network with Balanced Excitation and Inhibition during Motor Patterns Has High Resilience to Structural Division.” *The Journal of Neuroscience: The Official Journal of the Society for Neuroscience* 34 (8): 2774–84. https://doi.org/10.1523/JNEUROSCI.3349-13.2014.
Poo, Cindy, and Jeffry S. Isaacson. 2009. “Odor Representations in Olfactory Cortex: ‘Sparse’ Coding, Global Inhibition, and Oscillations.” *Neuron* 62 (6): 850–61. https://doi.org/10.1016/j.neuron.2009.05.022.
Prochazka, Arthur, and Sergiy Yakovenko. 2007. “The Neuromechanical Tuning Hypothesis.” *Progress in Brain Research* 165: 255–65. https://doi.org/10.1016/S0079-6123(06)65016-4.
Ringach, Dario L. 2004. “Mapping Receptive Fields in Primary Visual Cortex.” *The Journal of Physiology* 558 (Pt 3): 717–28. https://doi.org/10.1113/jphysiol.2004.065771.
Rutlin, Michael, Cheng-Ying Ho, Victoria E. Abraira, Colleen Cassidy, Ling Bai, C. Jeffery Woodbury, and David D. Ginty. 2014. “The Cellular and Molecular Basis of Direction

Selectivity of Aδ-LTMRs." *Cell* 159 (7): 1640–51. https://doi.org/10.1016/j.cell.2014.11.038.

Schillings, A. M., B. M. Van Wezel, and J. Duysens. 1996. "Mechanically Induced Stumbling during Human Treadmill Walking." *Journal of Neuroscience Methods* 67 (1): 11–17. https://doi.org/10.1016/0165-0270(95)00149-2.

Sherrington, Charles Scott. 1906. *The Integrative Action of the Nervous System*.

Sherrington, CS. 1910. "Remarks on the Reflex Mechanism of the Step" Brain 33: 1–25.

Sieber, Martin A., Robert Storm, Margaret Martinez-de-la-Torre, Thomas Müller, Hagen Wende, Katja Reuter, Elena Vasyutina, and Carmen Birchmeier. 2007. "Lbx1 Acts as a Selector Gene in the Fate Determination of Somatosensory and Viscerosensory Relay Neurons in the Hindbrain." *Journal of Neuroscience* 27 (18): 4902–9. https://doi.org/10.1523/JNEUROSCI.0717-07.2007.

Takakusaki, K., T. Habaguchi, J. Ohtinata-Sugimoto, K. Saitoh, and T. Sakamoto. 2003. "Basal Ganglia Efferents to the Brainstem Centers Controlling Postural Muscle Tone and Locomotion: A New Concept for Understanding Motor Disorders in Basal Ganglia Dysfunction." *Neuroscience* 119 (1): 293–308. https://doi.org/10.1016/s0306-4522(03)00095-2.

Tamamaki, Nobuaki, Yuchio Yanagawa, Ryohei Tomioka, Jun-Ichi Miyazaki, Kunihiko Obata, and Takeshi Kaneko. 2003. "Green Fluorescent Protein Expression and Colocalization with Calretinin, Parvalbumin, and Somatostatin in the GAD67-GFP Knock-in Mouse." *The Journal of Comparative Neurology* 467 (1): 60–79. https://doi.org/10.1002/cne.10905.

Tripodi, Marco, Anna E. Stepien, and Silvia Arber. 2011. "Motor Antagonism Exposed by Spatial Segregation and Timing of Neurogenesis." *Nature* 479 (7371): 61–66. https://doi.org/10.1038/nature10538.

Tuthill, John C., and Eiman Azim. 2018. "Proprioception." *Current Biology* 28 (5): R194–203. https://doi.org/10.1016/j.cub.2018.01.064.

Wehr, Michael, and Anthony M. Zador. 2003. "Balanced Inhibition Underlies Tuning and Sharpens Spike Timing in Auditory Cortex." *Nature* 426 (6965): 442–46. https://doi.org/10.1038/nature02116.

Wetzel, M. C., A. E. Atwater, J. V. Wait, and D. G. Stuart. 1976. "Kinematics of Locomotion by Cats with a Single Hindlimb Deafferented." *Journal of Neurophysiology* 39 (4): 667–78. https://doi.org/10.1152/jn.1976.39.4.667.

Wilent, W. Bryan, and Diego Contreras. 2005. "Dynamics of Excitation and Inhibition Underlying Stimulus Selectivity in Rat Somatosensory Cortex." *Nature Neuroscience* 8 (10): 1364–70. https://doi.org/10.1038/nn1545.

Wu, Haohao, Charles Petitpré, Paula Fontanet, Anil Sharma, Carmelo Bellardita, Rolen M. Quadros, Paulo R. Jannig, et al. 2021. "Distinct Subtypes of Proprioceptive Dorsal Root Ganglion Neurons Regulate Adaptive Proprioception in Mice." *Nature Communications* 12 (1): 1026. https://doi.org/10.1038/s41467-021-21173-9.

Zheng, Yang, Pin Liu, Ling Bai, James S. Trimmer, Bruce P. Bean, and David D. Ginty. 2019. "Deep Sequencing of Somatosensory Neurons Reveals Molecular Determinants of Intrinsic Physiological Properties." *Neuron* 103 (4): 598-616.e7.

DECLARATION OF INTERESTS

The authors declare no competing interest.

LEAD CONTACT AND MATERIALS AVAILABILITY

Further information and requests for resources should be directed to and will be fulfilled by the Lead Contact, Victoria E. Abraira (victoria.abraira@rutgers.edu).

EXPERIMENTAL MODEL AND SUBJECT DETAILS

Mouse lines used to target DRG neuron populations include *TH*^{2aCreER} (Jax#025614), *vGlut3*^{iresCre} (Jax#028534), *TrkB*^{CreER} (Jax#027214), PTGFR^{CreER} (Zheng et al. 2019; Lehnert et al. 2021), *Ret*^{CreER} (Luo et al. 2009), Split^{Cre} (Rutlin et al. 2014), *Advillin*^{Cre} (Jax#032536), Advillin^{CreER} (Jax#032027) and *PV*^{2aCreER} (Jax#028580). Mouse lines used to target spinal cord interneurons include *vGAT*^{irescre} (Jax#028862), *GAD2*^{Cherry} (Jax#023140), GAD67^{GFP} (Tamamaki et al. 2003), GlyT2^{GFP} (Miranda et al. 2022) , RoRB^{FlpO} (Jax#029590), RorB^{CreER}*,Satb2*^{CreER} (Hilde et al. 2016), *vGlut2*^{iresCre}(Jax#016963), *islet1*^{iresCre} (Jax#024242), Sim1^{iresCre} (Jax#006395), CCK^{iresCre} (Jax#012706), vGluT2^{YFP} (Jax#017978), and *Lbx1*^{Cre} (Sieber et al. 2007). To target Parvalbumin interneurons we used PV^{Tdtomato} (Jax#027395) and PV^{FlpO} (Jax#022730) mouse-lines. For visualization, and manipulation of target populations the following mouse lines were used: *R26*$^{LSL\text{-}FSF\text{-}tdTomato}$ (Ai65, Jax#021875), *R26*$^{LSL\text{-}FSF\text{-}synaptophysin\text{-}GFP}$ (*RC::FPSit,* Jax#030206), R26$^{FSF\text{-}SynGFP}$ (derived from RC::FPSit), *R26*$^{LSL\text{-}synaptophysin\text{-}tdTomato}$ (Ai34, Jax#012570), *R26*$^{LSL\text{-}tdTomato}$ (Ai9, Jax#007909), *R26*$^{LSL\text{-}tdTomato}$ (Ai14, Jax#007914),Tau$^{LSL\text{-}LacZ\text{-}FSF\text{-}DTR}$ (Gatto et al. 2021) *R26*$^{LSL\text{-}ChR2\text{-}YFP}$(Ai32, Jax#024109);*R26*$^{LSL\text{-}FSF\text{-}ChR2\text{-}YFP}$(Ai80, Jax#025109). ChAT^{eGFP} (Jax#007902) was used to target cholinergic interneurons and motor neurons , *Emx1*^{Cre} (Jax#005628) was used to target cortical neurons, and *Lbx1*^{Cre} (Acton et al. 2019) was used to identify dPVs genetic lineage and restrict PV expression to the deep dorsal horn. Transgenic mouse strains were used and maintained on a mixed genetic background (129/C57BL/6). Experimental animals used were of both sexes. With the exception of EMG recordings, housing, surgery, behavioral experiments and euthanasia were performed in compliance with Rutgers University Institutional Animal Care and Use Committee (IACUC; protocol #: 201702589). All mice used in experiments were housed in a regular light cycle room (lights on from 08:00 to 20:00) with food and water available ad libitum.

EMG recordings were performed at the lab of Dr. Turgay Akay (Dalhousie, Canada) according to the Canadian Council on Animal Care (CCAC) guidelines and approved by the local council on animal care of Dalhousie University. All mice used in experiments were housed in a regular light cycle room (lights on from 07:00 to 19:00) with food and water available ad libitum.

METHOD DETAILS

Tamoxifen treatment

Tamoxifen was dissolved in ethanol (20 mg/ml), mixed with an equal volume of sunflower seed oil (Sigma), vortexed for 5-10 min and centrifuged under vacuum for 20-30 min to remove the ethanol. The solution was kept at −80°C and delivered via oral gavage to pregnant females for

embryonic or postnatal treatment. For all analyses, the morning after coitus was designated as E0.5 and the day of birth as P0.

Immunohistochemistry and free- floating sections

Male and female P30-P37 mice were anesthetized with isoflurane and perfused transcardially (using an in-house gravity driven- perfusion system) with Heparinized- saline (~30 sec) followed by 15-20 minutes of 4% paraformaldehyde (PFA) in PBS at room temperature (RT). Vertebral columns were dissected and post-fixed in 4% PFA at 4°C for 2 hours (for c-fos and PV staining) or 24 hr. Sections were collected using a vibrating microtome (Leica VT1200S) and processed for immunohistochemistry (IHC) as described previously (Hughes et al., 2012). Unless otherwise mentioned, transverse sections (50-60 thick) were taken from the limb level lumbar spinal cord (LIV-VI). Free floating sections were rinsed in 50% ethanol (30 min) to increase antibody penetration, followed by three washes in a high salt PBS buffer (HS-PBS), each lasting 10 min. The tissue was then incubated in a cocktail of primary antibodies made in HS- PBS containing 0.3% Triton X-100 (HS-PBSt) for 48 at 4°C. Next, tissue was washed 3 times (10 minutes each) with HS-PBSt, then incubated in a secondary antibody solution made in HS-PBSt for 24 hr at 4°C. Immunostained tissue was mounted on positively charged glass slides (41351253, Worldwide Medical Products) and coverslipped (48393-195, VWR) with Fluoromount-G mounting medium (100241-874, VWR).

Image acquisition and analysis

Images were captured with a Zeiss LSM 800 confocal or a Zeiss axiovert 200M fluorescence microscope. Images for cell counts were taken with 10x or 20x air objectives, and images of synaptic contacts were taken with a 40x oil objective. ImageJ (cell count plug-in) was used for colocalization analysis of cell bodies. Imaris was used for synaptic analysis. For synaptic analysis of proprioceptive and cutaneous input onto dPVs, the fraction of each input was calculated relative to their sum. For synaptic analysis of dPVs output to target neurons, input was normalized to cell body area or dendrite length. Only puncta apposing a postsynaptic marker (Homer1 and Gephyrin for excitatory and inhibitory synapses, respectively) were included for analysis. Synaptic analysis was performed separately for somas and proximal dendrites (up to 50 um from the cell body). Imaris software was additionally used for measurement of the cell body/synaptic terminal's spatial coordinates (using the central canal and dorsal edge of the spinal cord as references). This data was then used to generate density plots (custom matlab script).

c-Fos induction

To decrease stress, at least 7 days prior the experiment, mice were transferred to a holding area adjacent to the testing room. 6-8 weeks old $vGAT^{Cre}$;$Tau^{LSL\text{-}LacZ}$ mice were randomly placed in one of three groups: control (n=4), swim (n=4) and walk (n=5). All mice were habituated to the testing room for 30 minutes. Control mice were kept in their homecage for 60 minutes. "Walk" group walked on a treadmill (Mouse Specifics, Inc, Boston, MA, USA) at 20 cm/s for 2 x 20

minutes with a 5 minute break. “Swim” group were kept in a swim tank for 4 x 10 minutes with 5 minutes breaks. 60 minutes following the completion of the task, mice were anesthetized with isoflurane and perfused for immunohistochemistry. Sections stained with chicken-ß-galactosidase (ab9361, abcam), mouse- NeuN (MAB377, millipore), and rabbit- c-fos (226003, Synaptic Systems) were used to acquire 20x images of the entire hemisection, stitches with zen. These images were used for quantification of c-fos expressing neurons (normalized to total NeuN) by lamina (figure 1) and cfos expressing inhibitory (vGAT+cfos+NeuN+) and excitatory (vGAT-cfos+NeuN-) neurons in the medial portion of laminas 4-5 (Figure 2). Alternate sections from the same animals stained with Guinea pig-PV (PV-GP-Af1000, frontier institute) and c-fos, were used to acquire 20x images of the deep dorsal horn to quantify the fraction of dPVs that express cfos in each of the 3 conditions. All images were acquired with the Zeiss LSM 800 confocal microscope. 3-6 images from each mouse were used for quantification.

CTb muscle injection

PV^{FlpO};Lbx1^{Cre};Rosa$^{LSL\text{-}FSF\text{-}SynaptophysinGFP}$ mice were anesthetized (5% induction, 2-3% maintenance), and the hair above one of their hindlimbs was shaved. The skin was wiped with 70% ethanol and cut to expose hindlimb muscles. Injections were made into hindlimb knee extensor Vastus Lateralis, knee flexor Biceps Femoris (BCP), ankle extensor Lateral Gastrocnemius (Gs), and ankle flexor Tibialis Anterior (TA). Injection of 0.125% Alexa-Ctb was made into 2-3 sites along each muscle. Animals were perfused 5d after tracer injection and tissue was processed for immunohistochemistry as described above. Free floating sections were immunostained with chicken-GFP and mouse- Gephyrin primary antibodies, and appropriate secondary antibodies. 40x or 63x high resolution images of CTb- labeled motor neurons were taken at the Zeiss LSM 800 confocal microscope and ImageJ was used for synaptic analysis. Synaptic analysis included 11 VL-motor neurons (from 2 animals), 10 Gs- motor neurons (from 2 animals), 9 TA- motor neurons (from 1 animal), and 14 LG- motor neurons (from 1 animal).

Electrophysiology

Recordings were made from male and female mice. Mice were anesthetized with ketamine (100 mg/kg i.p), decapitated, and the lumbar enlargement of the spinal cord rapidly removed in ice-cold sucrose substituted artificial cerebrospinal fluid (sACSF) containing (in mM): 250 sucrose, 25 NaHCO3, 10 glucose, 2.5 KCl, 1 NaH2PO4, 6 MgCl2, and 1 CaCl2. Sagittal or transverse slices (200µm thick) were prepared using a vibrating microtome (Leica VT1200S). Slices were incubated for at least 1hr at 22-24°C in an interface chamber holding oxygenated ACSF containing (in mM): 118 NaCl, 25 NaHCO3, 10 glucose, 2.5 KCl, 1 NaH2PO4, 1 MgCl2, and 2.5 CaCl2.

Following incubation, slices were transferred to a recording chamber and continually superfused with ACSF bubbled with Carbogen (95% O2 and 5% CO2) to achieve a pH of 7.3-7.4. All recordings were made at room temperature (22-24°C) and neurons visualized using a Zeiss Axiocam 506 color camera. Recordings were acquired in cell-attached (holding current = 0mV), voltage-clamp (holding potential -70mV), or current-clamp (maintained at −60mV). Patch pipettes (3-7 MΩ) were filled with a potassium gluconate-based internal solution containing (in mM): 135 C6H11KO7, 8 NaCl, 10 HEPES, 2 Mg2ATP, 0.3 Na3GTP, and 0.1 EGTA, (pH 7.3,

adjusted with KOH, and 300 mOsm) to examine AP discharge and excitatory synaptic transmission. A cesium chloride-based internal solution containing (in mM): 130 CsCl, 10 HEPES, 10 EGTA, 1 $MgCl_2$, 2 Na-ATP, 2 Na-GTP, and 5 QX-314 bromide (pH 7.3, adjusted with CsOH, and 280 mOsm) was used to record inhibitory synaptic transmission. No liquid junction potential correction was made, although this value was calculated at 14.7 mV (22°C). Slices were illuminated using an X-CITE 120LED Boost High-Power LED Illumination System that allowed visualization of Td-Tomato expressing dPVs with TRITC filters, and visualization of GFP fluorescence and ChR2 photostimulation using FITC filter set.

AP discharge patterns were assessed in the current clamp from a membrane potential of −60 mV by delivering a series of depolarizing current steps (1 s duration, 20 pA increments, 0.1 Hz), with rheobase defined as the first current step that induced AP discharge. For optogenetic circuit mapping, photostimulation intensity was suprathreshold (24 mW), duration 1 ms (controlled by transistor-transistor logic pulses), 0.1 Hz. This ensured generation of action potential discharge in presynaptic populations and allowed confident assessment of postsynaptic currents in recorded neurons.

All data were amplified using a MultiClamp 700B amplifier, digitized online (sampled at 20 kHz, filtered at 5 kHz) using an Axon Digidata 1550B, acquired and stored using Clampex software. After obtaining the whole-cell recording configuration, series resistance, input resistance, and membrane capacitance were calculated (averaged response to -5mV step, 20 trials, holding potential -70mV).

Electrophysiology Analysis

All data were analysed offline using AxoGraph X software.

AP discharge was classified according to previously published criteria (Browne et al. 2020). In the analysis of AP discharge, individual APs elicited by step-current injection were captured using a derivative threshold method (dV/dt > 15 V/second) with the inflection point during spike initiation defined as the AP threshold. Individual AP properties for each neuron were assessed from the first spike generated at rheobase. AP latency was measured as the time difference between the stimulus onset and AP threshold. The difference between the AP threshold and its maximum positive peak was defined as the AP peak. AP half-width was measured at 50% of AP peak. AP rise and decay time were measured from 10-90% of peak. AP afterhyperpolarization (AHP) amplitude was taken as the difference between the AP threshold and the maximum negative peak following the AP. AHP half-width was measured at 50% of AHP peak. AP threshold adaptation was determined by dividing the AP threshold of the last AP by the AP Threshold of the first AP evoked by a step-current. AP number was the number of spikes discharged in the entire response. Instantaneous frequency was the average instantaneous frequency across a step-current.

Optogenetically-evoked excitatory postsynaptic currents (oEPSCs) and inhibitory postsynaptic currents (oIPSCs) were measured from baseline, just before photostimulation. The peak amplitude of responses was calculated from the average of 10 successive trials. A number of parameters were considered for determining whether a photostimulation-evoked synaptic input

was monosynaptic or polysynaptic. The latency of oPSCs was measured as the time from photostimulation to the onset of the evoked current. The “jitter” in latency was measured as the standard deviation in latency of 10 successive trials. Importantly, the latency of monosynaptic inputs was much shorter, there was minimal jitter in the onset of responses between trials, and reliability (percentage of photostimulation trials to evoke a response) was higher than those deemed polysynaptic inputs. To assess the contribution of different neurotransmitter systems to photostimulation responses, various synaptic blockers were sequentially applied.

Diphtheria Toxin preparation and delivery

DTx was dissolved in 1xPBS to 100 ug/ml and kept as 15 ul aliquot at −20°C. On the day of injection, DTx was diluted 1:10 in a hyperbaric solution (filtered 0.9% NaCl, 8% dextrose) as described in (Albisetti et al. 2019). P21-P28 mice carrying the PV^{FlpO};Lbx^{1Cre};$Tau^{LSL\text{-}FSF\text{-}DTR}$ ($dPVs^{abl}$) or PV^{FlpO};$Tau^{LSL\text{-}FSF\text{-}DTR}$ ($dPVs^{norm}$) alleles, received Diphtheria Toxin (DTx, D0564-1MG, Sigma) on day 1 and 3 (5 ul of 10 ug/ml DTx, overall 50 ng) through intrathecal (I.T.) injection to the L5-L6 intervertebral space. DTx was delivered with a 25 ul Hamilton syringe (72310-388) with a 30 G needle and performed as previously described (D. Li et al. 2019). Briefly, mice were anesthetized with isoflurane and the hair above their lower back was removed with nair. Under anesthesia, exposed skin was wiped with 70% ethanol. Next, mice were held firmly by the pelvic girdle with their skin taut in one hand, while the other hand was used to gently rotate the base of the tail to find the midline of the spine. Needle was inserted through the skin along the midline, between the pelvic girdles to the L5-L6 intervertebral space. An occurrence of a sudden tail indicated successful entry into the intradural space.

Quantification of DTx mediated ablation

Following behavioral testing, 9 PV^{FlpO};Lbx^{1Cre};$Tau^{LSL\text{-}FSF\text{-}DTR}$ and 6 PV^{FlpO};$Tau^{LSL\text{-}FSF\text{-}DTR}$ mice were perfused, their spinal cord and cerebellum were dissected, and sectioned using a vibrating microtome (Leica VT1200S). For consistency, sections were collected at the levels of the mid cervical enlargement, mid thoracic, mid lumbar enlargement, and the midline of the cerebellum. Sections were immunostained with Guinea pig-PV and mouse- NeuN, and 20x images were taken using the Zeiss axiovert 200M fluorescence microscope. For quantification, 3 spinal cord and 2 cerebellum images were used. PV neurons were counted in the superficial dorsal horn (sPVs), deep dorsal horn (dPVs) and molecular layer of the cerebellum. sPVs were normalized to NeuN, dPVs were normalized to sPVs (to account for difference in staining success), and PV neurons in the molecular layer were normalized to area.

Behavioral testing

7-12 weeks old male and female PV^{FlpO};Lbx^{1Cre};$Tau^{LSL\text{-}FSF\text{-}DTR}$ and PV^{FlpO};$Tau^{LSL\text{-}FSF\text{-}DTR}$ mice were used for behavior testing following DTx injection (P21-P28).The experimenter was blind to the genotype of the animals. For all behavior assays, mice were transferred to the holding area adjacent to the behavior rooms at least 7 days prior testing. On the day of training/testing, mice were transferred to the behavior room for a 30 minute habituation.

Balance beam

Mice were trained for 2 days to cross an elevated, 1m long, wide (10 mm) rectangular beam. On the test day, mice were allowed to cross wide and narrow (10 mm and 5 mm) rectangular and circular beams. Individual trials were video-recorded using a 30 fps camera (GoPro) , capturing mouse performance from the side. A mirror positioned on the side of the mouse that did not face the camera was used to capture the performance of the contralateral leg. Each mouse performed 3 consecutive trials on each beam and the total number of slips, time to cross the beam were calculated. All beams were custom made in-house.

Horizontal ladder test

Mice were trained for 2 days to cross a 60 cm long, horizontal ladder (Maze Engineers, Skokie, USA). The ladder was elevated from the ground with two cages, a neutral cage at the star and homecage at the end, to motivate mice to cross the ladder. The ladder consisted of 2 transparent side walls, with drilled holes in regularly spaced, 1 cm intervals, allowing for the insertion of metal bars (0.3 cm wide) at different spacing. During training days, ladder rungs were spaced 1 cm apart and mice performed 3-5 consecutive trials of ladder crossing. On the test day, mice performed 3-5 trials on a regular pattern ladder (rungs 1 cm apart) and 3 trials on an irregular pattern ladder where some rungs were spaced 2 cm apart. 3 different patterns (A,B, and C) were used for each mouse which were the same across mice. Mice were allowed to rest for 2-3 hours between the testing on the regular and the irregular pattern ladder. A camera (specifics) located to the side of the mouse and positioned in an angle to capture the performance of all 4 paws was used to videotype mouse performance at 30 fps. Videos were analyzed frame by frame to quantify the number of slips and hops (defined by simultaneous forward motion of the two hindlimbs while forelimbs hold the rungs.

Rotarod test

The rotarod assay lasted for 5 days. On day 1 mice were habituated to the apparatus and placed on the rotarod, rotating at 4 rpm. for a maximum of 3 minutes On following days, mice were put on the accelerating rotarod (4-40 rpm, maximum of 3 minutes), and their latency to fall and speed at fall were measured. Mice performed 4 trials each day, with a break of 15-20 minutes between trials.

Analysis of step cycle parameters

Mice were forced to walk on a motorized treadmill (Mouse specifics, inc.) with a transparent belt at speeds 5-100 cm/s for 2 days. Each mouse had to exhibit a minimum of 3 second walk at a certain speed for it to be included in the analysis. On day 2, mice were given one more chance to walk at speeds they failed at on the first day. A high speed camera (165 fps) located underneath the belt, was used to record mice paw placement. A custom-developed software was used to calculate the area paw in contact with the belt, for each paw, in each video frame, as described in (Hampton et al. 2004). We then used this data to calculate (in house matlab script) the duration of stance (when paw area>0), swing (paw area=0), stride (summed swing and stance duration) and the stride frequency (the number of strides per second) of each limb.

Estimation of joint angles

The day before the test, mice were anesthetized and the hair above their right hindlimb was removed with nair. On the day of the test, mice were habituated to the test room for 30 minutes, then briefly anesthetized and 5 marker dots (oil-based white marker, 208423, Office Depot) were placed on key hindlimb landmarks (iliac crest, hip, ankle, metatarsophalangeal/MTP, and toe). Due to excess skin above the knee, knee joint location was calculated post-hoc using measurements of tibia and femur length. 6 calibration points with a known distance (5 mm apart) were put on the upper right side of the treadmill, which were later used for post-hoc analysis. Mice were placed on the treadmill to recover from anesthesia (several minutes), after which a high speed camera (PROMON U1000, AOS Technologies, AG, Switzerland) recorded their performance from the lateral side, at 415 fps. Videos were analyzed with DeepLabCut for 2D estimation of joint marker location in each video frame as described in (Mathis et al. 2018). Briefly, 2 separate models were created for the calibration points and joint markers. Each model was trained with a random subset of videos. An average of 125 frames were extracted and labeled by clustering based on similarities in visual appearance (k-means). The models were trained with a ResNet-50-based neural network for an average of 300,000 training iterations. Using a p-cutoff of 0.9, the training datasets were shuffled with the default 95/5 split for training and testing, and evaluated with an average train error: 2.16 pixels, test: 2.38 pixels. Incorrectly labeled or missing labels were detected and corrected via extraction of outlier frames, refinement of label errors, and subsequent retraining of the model. With minimal retraining, models were able to estimate and yield 2D pixel coordinates. We used the estimated pixel coordinates of the calibration points to calculate a pixel- to- mm conversion value, then estimated the location of the knee joint in each frame using the lengths of the femur and tibia. A custom semi- automatic matlab script was used to identify the beginning of stance (the first frame on which the toe touches the ground) and swing (the first frame of paw lift-off) in each step cycle (defined from the beginning of stance to the end of swing). The complete data set of the estimated location of all 6 joints was used to generate stick diagrams of hindlimb pose and calculate the instantaneous joint angle between every three consecutive markers, throughout the step cycle.

Construction of EMG electrodes

EMG electrodes were made using multi-stranded, teflon coated annealed stainless-steel wire (A-M systems, catalog number 793200). The construction of the EMG electrode and nerve cuff was previously described in detail (Pearson, Acharya, and Fouad 2005; Akay et al. 2006; 2014). Two nerve cuff electrodes and six EMG recording electrodes were attached to the headpiece pin connector (female, SAM1153-12; DigiKey Electronics Thief River Falls, MN) and covered with 3D printed cap.

EMG electrode implantation surgeries

Experiments were conducted on males and females (4-5 month-old), PV^{FlpO}/Lbx^{1Cre};$Tau^{LSL\text{-}FSF\text{-}DTR}$ (dPVs^{norm}, n=9) and PV^{FlpO};Lbx^{1Cre};$Tau^{LSL\text{-}FSF\text{-}DTR}$ (dPVs^{abl}, n=6) mice.

All surgeries were performed in aseptic conditions and on a warm water-circulated heating pad maintained at 42°C. Each mouse received an electrode implantation surgery as previously described (Laflamme and Akay 2018; Laflamme, Ibrahim, and Akay 2022). Briefly, animals were anesthetized with isoflurane (5% for inductions, 2% for maintenance of anesthesia), ophthalmic eye ointment was applied to the eyes, and the skin of the mice was sterilized with three-part skin scrub using hibitane, alcohol and povidone-iodine. Prior to each surgery, buprenorphine (0.03 mg/kg) and meloxicam (5 mg/kg) were injected subcutaneously as analgesics while the

animals were still under anesthesia. Additional buprenorphine injections were performed in 12-hour intervals for 48 hours.

A set of six bipolar EMG electrodes and two nerve stimulation cuffs were implanted to each mouse as the following: small incisions were made on the shaved areas (neck and both hind legs), and each bipolar EMG electrode and the nerve cuff electrodes were led under the skin from the neck incisions to the leg incisions, and the headpiece connector was stitched to the skin around the neck incision. EMG recording electrodes were implanted into the left knee flexor (semitendinosus, St_l), ankle flexor (tibialis anterior, TA_l) and extensor (gastrocnemius, Gs_l) as well as the right knee flexor (semitendinosus, St_r) and extensor (Vastus Lateralis, VL_r) and the left ankle extensor (gastrocnemius, Gs_r). Nerve stimulation electrodes were implanted in the left saphenous nerve and right sural nerve to evoke cutaneous feedback. After surgery, the anesthetic was discontinued, and mice were placed in a heated cage for three days before returning to a regular mouse rack. Food mash and hydrogel were provided for the first three days after the surgery. Any mouse handling was avoided until mice were fully recovered, and the first recording session started at least ten days after electrode implantation surgeries.

EMG recording sessions

After animals fully recovered (~10 days) from electrode implantation surgeries, recording session went as follows: Under brief anesthesia with isoflurane, a wire to connect the headpiece connector with the amplifier and the stimulation insulation units (ISO-FLEX -AMPI, Jerusalem, Israel or the DS4 -Digitimer, Hertfordshire, United Kingdom) were attached to the mouse. The anesthesia was discontinued, and the mouse was placed on a mouse treadmill (model 802; custom built in the workshop of the Zoological Institute, University of Cologne, Germany). The electrodes were connected to an amplifier (model 102; custom built in the workshop of the Zoological Institute, University of Cologne, Germany) and a stimulus isolation unit. After the animal fully recovered from anesthesia (at least five minutes), the minimal (threshold) current necessary to elicit local reflex responses in the ipsilateral leg was determined by injecting a double impulse of 0.2 ms duration into the saphenous nerve (average ±SD threshold current: 436.4 μA ±396; range: 120-1300 μA) and the sural nerve (average ±SD threshold current: 117.6 μA ±83.4; range: 28-230 μA) of $dPVs^{norm}$, and the saphenous nerve (average ±SD threshold current: 215 μA ±157.9; range: 64-450 μA) and the sural nerve (average ±SD threshold current: 253.3 μA ±127.5; range: 130-500 μA) of $dPVs^{abl}$. Following the determination of threshold currents, the current injected into the sural and saphenous nerve was set as either 1.2 times the local reflex threshold current (1.2 X threshold) or five times the local reflex threshold current (5 X threshold).

EMG signals from six muscles of the right and left leg were simultaneously recorded (sampling rate: 10,000 kHz). For the 1- nerve stimulation assay, saphenous or sural nerve were electrically stimulated, while for the 2- nerve stimulation assay, both nerves were stimulated at varying delays (0,5,15,15,20,25,30,35,40,45, or 50 ms). Paired stimulation of both legs at different delays provide evidence of an inhibitory period if there is a suppression of the motor responses from one leg following stimulation of the other leg. Nerve stimulations (five 0.2ms impulses at 500 Hz) were applied using the ISO-FLEX (AMPI, Jerusalem, Israel) and DS4 (Digitimer,

Hertfordshire, United Kingdom) stimulation insulation units. Stimulation protocols were recorded while the mice were resting on the treadmill. EMG signals were amplified (gain 100), band-pass filtered from 400 Hz to 5 kHz, and stored on the computer using Power1410 interface and Spike2 software (Cambridge Electronic Design, Cambridge, United Kingdom).

Analysis of EMG responses

EMG analysis response was done using Spike2 software (Cambridge Electronic Design, Cambridge, United Kingdom). Response latency was quantified for each stimulation and then averaged for each mouse. Inhibition quantification was performed on a delay in which the peak amplitude of the expected response is located between 10-20ms after the second nerve stimulation as a latency is shown to involve an inhibitory pathway (Laflamme and Akay, 2018; Laflamme et al. 2022). Every muscle inside a single mouse was treated separately to provide the best delay for each case. Average expected response was then compared to single paired stimulation of the selected delay. When the average expected response possesses a higher amplitude than the paired stimulation, it was categorized as an inhibition.

QUANTIFICATION AND STATISTICAL ANALYSIS

All data are reported as mean values ± s.e.m. Behavioral assays were repeated several times (3 to 10 times depending on the experiment) and averaged per animal. Statistical analysis was performed in GraphPad Prism (USA) or Matlab, using two-sided paired or unpaired Student's t-tests, one-way ANOVA for neuromorphological evaluations with more than two groups, and one- or two-way repeated-measures ANOVA for functional assessments, when data were distributed normally. Post hoc Tukey’s or Bonferroni test was applied when appropriate. The significance level was set as $p < 0.05$. The nonparametric Mann-Whitney or Wilcoxon signed-rank tests were used in comparisons of <5 mice. Statistics were performed over the mean of animals. For the analyses of step cycles and joint angles (Fig4D-H, Supp Fig X), all cycles/joint angles from all mice were used and statistical analysis was performed with a linear mixed effects regression model with mouse ID as a random effect.

DATA AND CODE AVAILABILITY

Data are available upon request from the Lead Contact, Victoria E. Abraira (victoria.abraira@rutgers.edu).

Figures

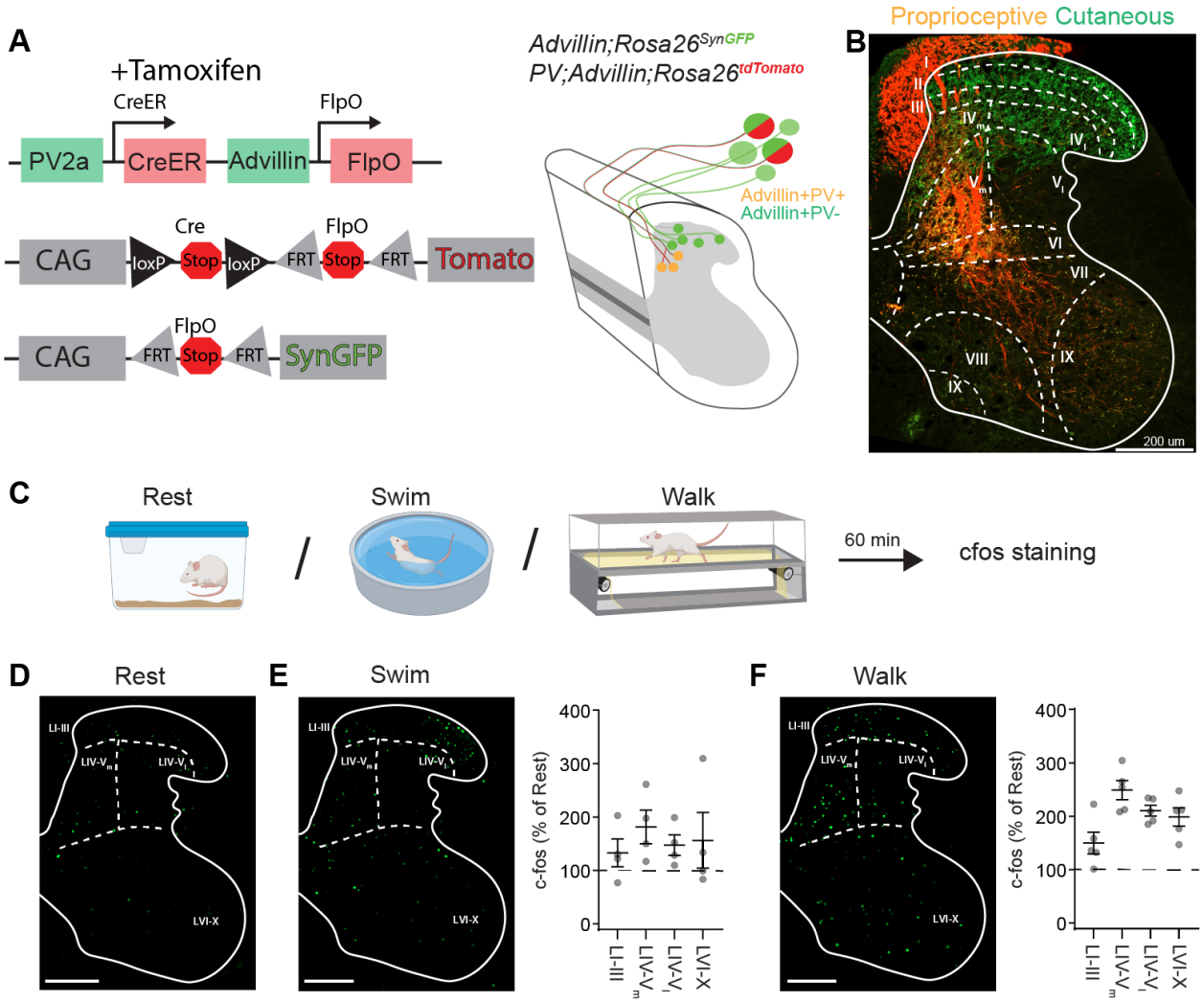

Figure 1. The medial deep dorsal horn, a region for convergence proprioceptive and cutaneous input, is recruited in locomotion. A) Left- intersectional genetic approach to label cutaneous and proprioceptive input in the mouse. Right- *PV^{2aCreER};Advillin^{FlpO};Rosa$^{LSL\text{-}FSF\text{-}Tomato}$/Rosa$^{FSF\text{-}SynGFP}$* mice have proprioceptor fibers (PV+Advillin+) labelled in red and all sensory terminals (Advillin+) in green. In the spinal cord, proprioceptors terminals are identified by both green and red fluorescence (yellow), while cutaneous terminals are identified by green fluorescence alone. **B)** Representative transverse section of limb level lumbar spinal cord from the genetic intersection in A, showing convergence of cutaneous and proprioceptive input in the medial part of laminas IV-V. scale bar: 200 µm **C)** Scheme of experiment used to identify spinal cord regions recruited during locomotion. Mice performed one of 3 tasks: rest, swimming or walking. 60 minutes following the completion of the task, tissue was perfused and processed for c-fos immunohistochemistry. **D-F)** c-fos expression is increased in the medial part of laminas IV-V during locomotion. Genetic cross used: *vGA^{TiresCre};Rosa$^{LSL\text{-}Tomato}$*. **D, E-left, F-left)** Representative images depicting c-fos expression in the rest (D), swim (E-left), and walk (F-left) condition. **E-right, F-right)** c-fos expression in the

swim (E-right) and walk (F-right) conditions, across lamina groups (LI-III, LIIV-V_{Medial}, LIIV-$V_{Lateral}$, and LVI-X). cfos is shown as a percentage of control.

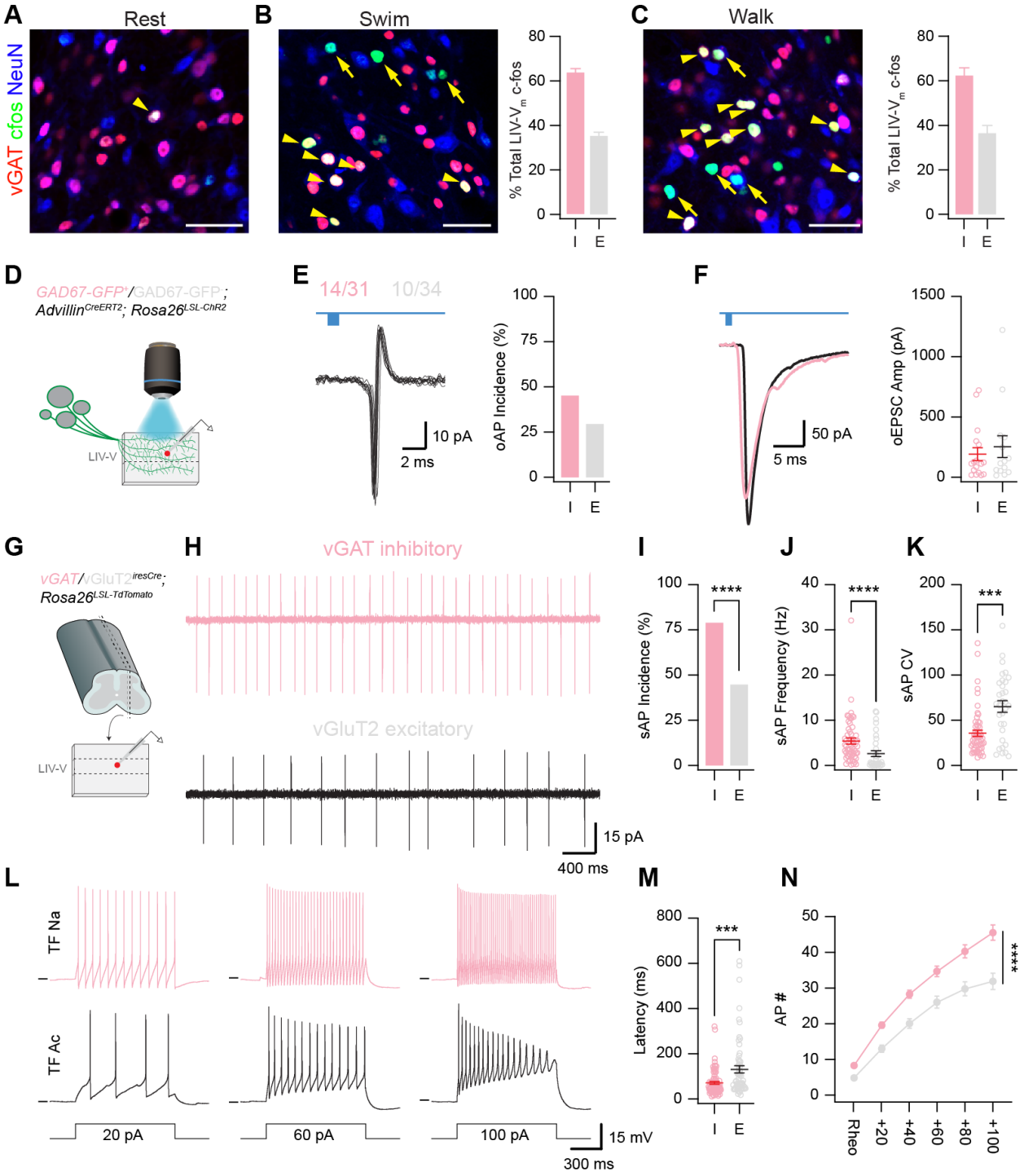

Figure 2. DDH Inhibitory interneurons are active during locomotion and exhibit excitable electrophysiological profiles. A-C) *vGAT^{iresCre};Rosa$^{LSL\text{-}Tomato}$* mice performed one of 3 tasks:

rest (A), swimming (B) or walking (C) and their tissue was processed for c-fos (green), vGAT (red) and NeuN (blue) immunostaining. **A,B-left, C-left)** Representative 20x confocal images, zoomed-in on the medial deep dorsal horn, show c-fos expressing inhibitory (cfos+vGAT+NeuN+, yellow arrowheads) and excitatory (cfos+vGAT-NeuN+, yellow arrows) neurons in the rest (A), swim (B-left), and walk (C-left) conditions. scale bars: 40 µm. **B-right, C-right)** Percentage c-fos expressing neurons that are inhibitory (I) and excitatory (E) in the swim (left) and walk (right) conditions. **D)** Schematic of conditions for sensory afferent photostimulation. **E)** Cell-attached voltage clamp recording showing 10 consecutive traces of optically evoked action potential discharge (left) and oAP incidence (right). **F)** Whole-cell voltage-clamp recording showing average of 10 consecutive traces following sensory afferent stimulation (left) and group data for oEPSC amplitude (right). Mann-Whitney test, $p = 0.6811$. **G)** Schematic of conditions for electrophysiological comparison of inhibitory and excitatory neurons. **H)** Cell-attached voltage clamp recording showing spontaneous AP discharge in inhibitory (pink) and excitatory (black) neurons. **I)** Inhibitory neurons exhibited higher sAP incidence. I vs. E, **** $p < 0.0001$; **J)** higher sAP frequency. Mann-Whitney test, ****$p < 0.0001$; **K)** and lower sAP coefficient of variation. Mann-Whitney test, ***$p = 0.0003$. **L)** Representative responses of inhibitory (pink, top) and excitatory (black, bottom) to depolarizing current injection. **M)** Inhibitory interneurons exhibited lower latency to 1st AP. Mann-Whitney test, ***$p = 0.0003$; **N)** and fired more APs in response to current injection. 2-way ANOVA, ****$p < 0.0001$.

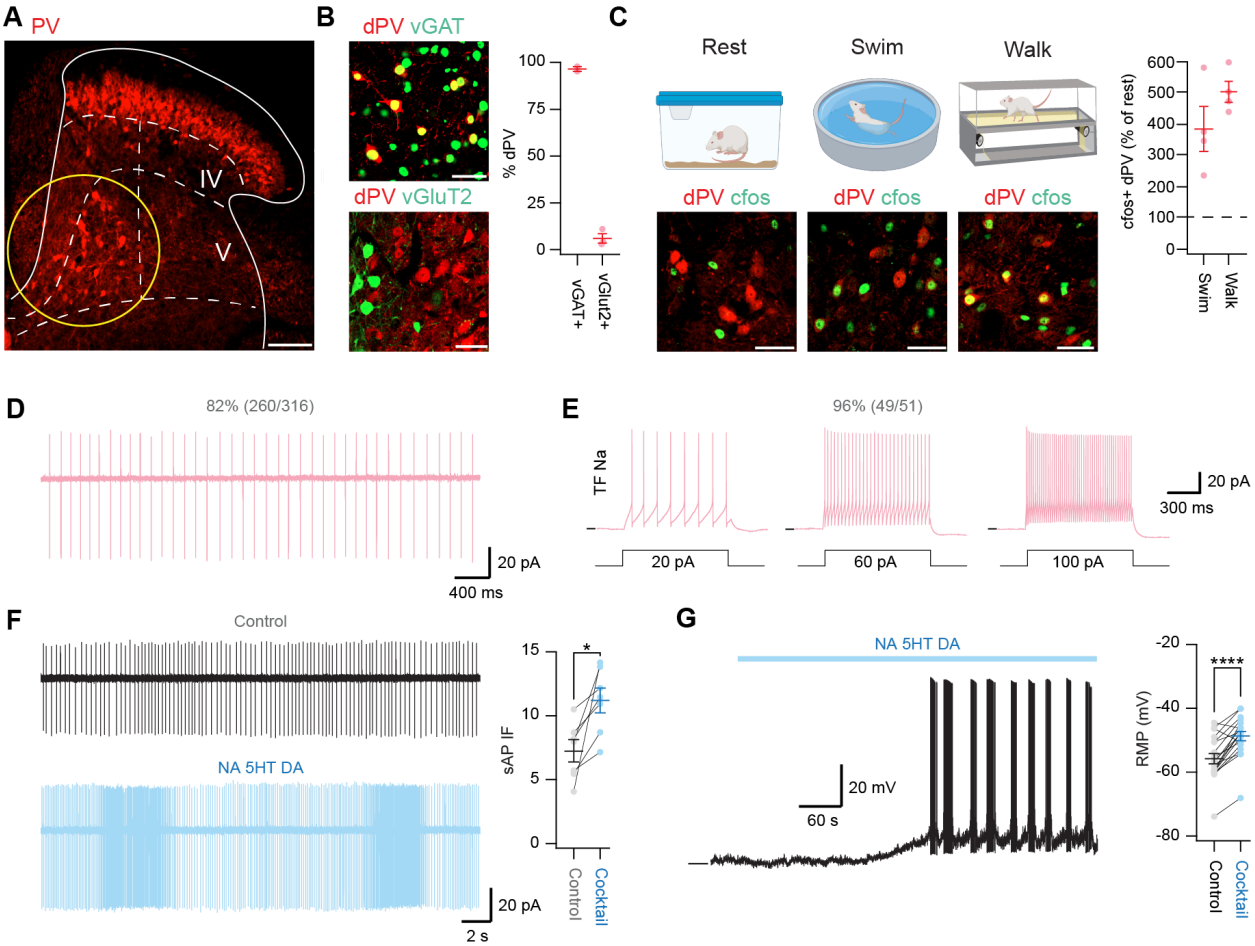

Figure 3. dPVs are active during locomotion. A) Transverse, lumbar section of PV^{TdTomato} BAC transgenic shows the presence of PV expressing interneurons in the deep dorsal horn (dPVs, in yellow circle). Scale bar: 100 µm. **B)** dPVs are inhibitory neurons. Left- representative images demonstrating colocalization of dPVs (PV+, red) with top- inhibitory (vGAT+, green) and bottom- excitatory (vGluT2+, green) interneurons. Genetic crosses used for this analysis: *vGAT^{Cre};Tau$^{LSL\text{-}LacZ}$;PVTdTomato* (6 slices from 2 animals), and vGluT2^{YFP};PV^{TdTomato} (6 slices from 3 animals) for colocalization with inhibitory and excitatory interneurons, respectively. Scale bar: 40 µm. **C)** Left, top- schematic of c-fos experiment used to quantify cfos expressing dPVs in different tasks. Left, bottom- 20x confocal images zoomed-in on the medial portion of laminas IV-V. Images show dPVs (red) and cfos (green) in the rest (left), swim (middle) walk (right) conditions. Scale bar: 40 µm. Right- Quantification of c-fos expressing dPVs in swim and walk. cfos is shown as a percentage of control. **D)** Cell-attached voltage clamp recording showing dPVs (82%) exhibit spontaneous AP discharge. **E)** Representative traces of dPV response to depolarizing current injection. **F)** Representative traces (left) and grouped data (right) showing dPV sAP frequency is increased following addition of NA, 5HT, and DA. Paired t-test, * $p = 0.0142$. **G)** NA, 5HT, and DA evoked depolarization (group data, right) evoked rhythmic discharge in a subset of dPVs (left). Paired t-test, **** $p < 0.0001$.

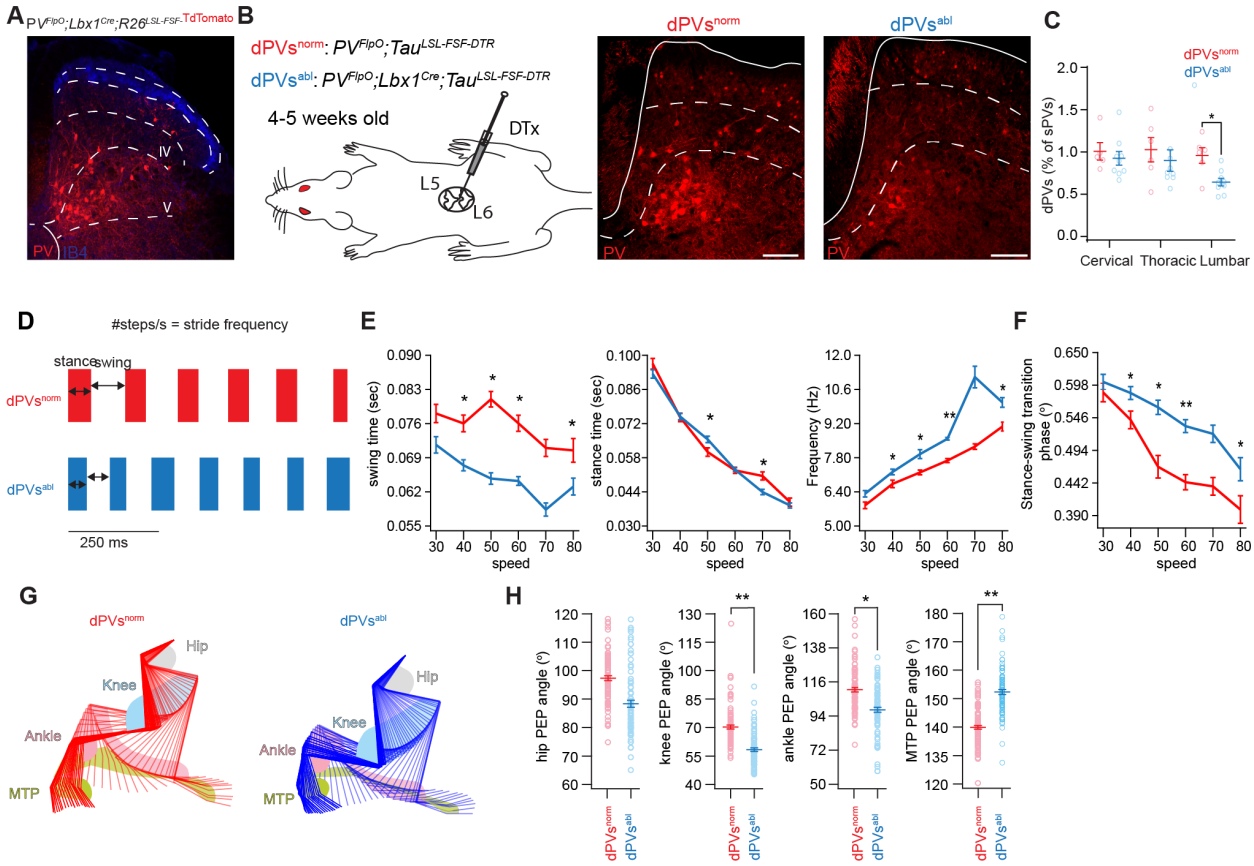

Figure 4. dPVs ablation alters stride frequency and joint kinematics. A) Strategy for dPVs ablation. *PV^FlpO*;Lbx1^Cre;*Tau^LSL-FSF-DTR* and PV^FlpO;Tau^LSL-FSF-DTR were injected with 50 ng Diphtheria toxin (DTx), delivered intrathecally (I.T.) into the L5-L6 intervertebral space to generate animals with ablated dPVs (dPV^abl) and non-ablated dPVs (dPV^norm). **B)** Transverse section demonstrating PV neurons in L4 spinal cord of dPV^norm (left) and dPV^abl (right). Scale bar: 100 µm. **C)** Quantification of dPVs (normalized to superficial PVs) in dPV^abl and dPV^norm throughout the cervical, thoracic and lumbar segments. **D-F)** Comparison of step cycle parameters of dPV^norm (red) and dPV^abl (blue) calculated from the data extracted by DigiGait™. **D)** Example stepping of the lateral hindlimb at 60 cm/s shows a shorter swing and increased step frequency in dPV^abl (blue). **E)** Comparison of swing duration (left), stance duration (middle) and step frequency (right) of the hindlimbs of dPV^norm (red) and dPV^abl (blue) at 30-80 cm/s, show consistent decrease in swing duration and increase in stride frequency. **F)** Quantification of stance to swing transition phase at 30-80 cm/s (data from lateral hindlimb) shows an increase in dPV^abl phase of transition. G-H) Estimation of joint angles during stepping of dPV^norm and dPV^abl. **G)** Example stick diagram of a step performed by dPV^norm (left) and dPV^abl (right) suggest changes in angle during surface contact (stance). **H)** comparison of the angle at the posterior extreme position (PEP, transition from stance to swing) shows hyperflexion of the knee and ankle and hyperextension of the MTP. Statistical analysis for dPV ablation (C) was done using Mann Withney test. Statistical analysis of step cycle (E-F) parameters and joint angles (H) was

performed with a linear mixed effects regression model with mouse ID as a random effect (D-H_ with *p < 0.05 and **p < 0.005. Graphs show average +S.E.M. blue and red denote dPV^{norm} and dPV^{abl}, respectively.

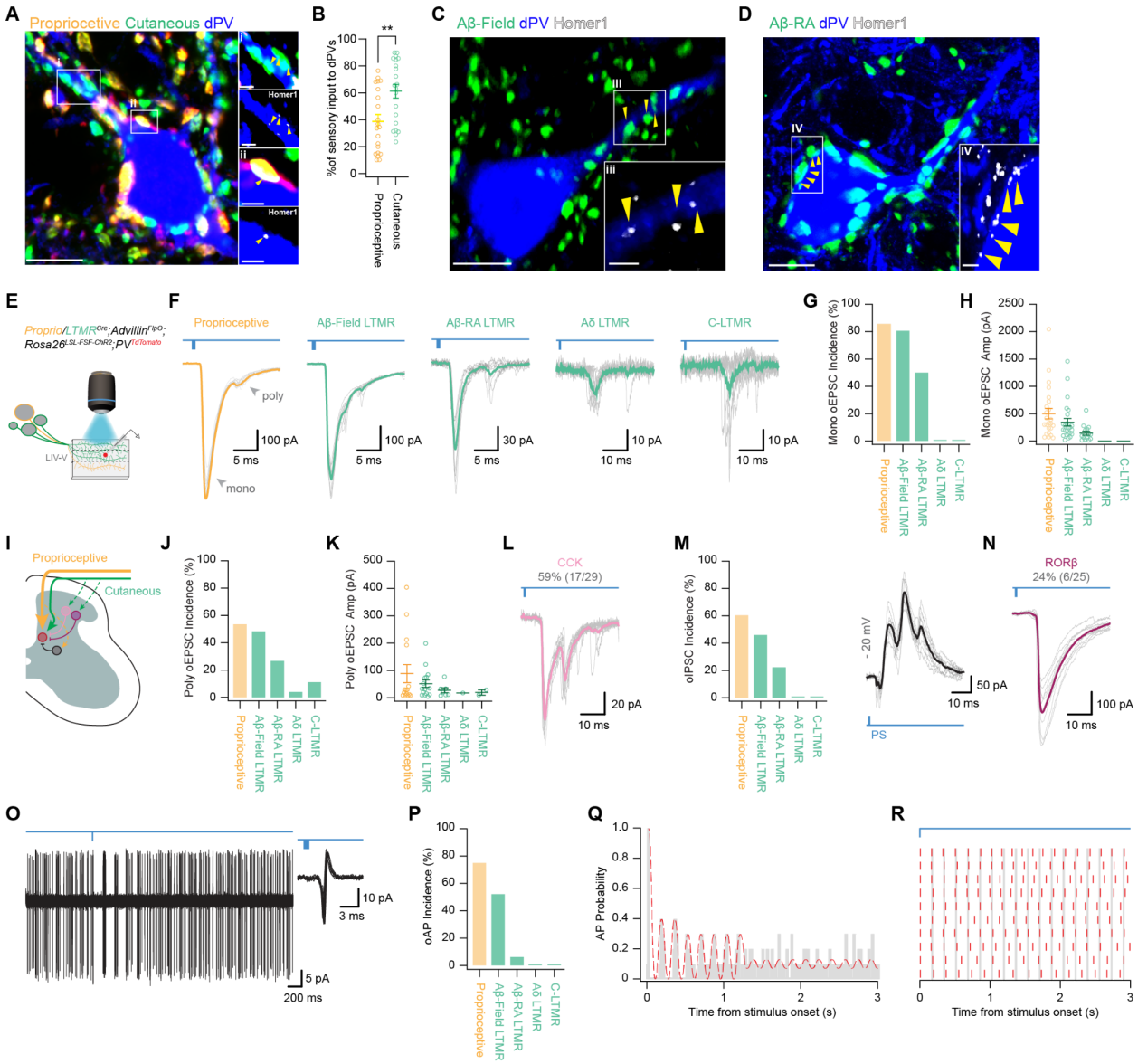

Figure 5. dPVs process convergent proprioceptive and cutaneous sensory inputs. A) 40x confocal image demonstrates a single dPV neuron surrounded and in contact with cutaneous (green) and proprioceptive (yellow) puncta. Genetic intersection: *PV^{2aCreER};Advillin^{FlpO};Rosa$^{LSL-FSF-TdTomato}$/Rosa$^{FSF-SynGFP}$*. Scale bar: 10μm. i,ii) cutaneous (i) and proprioceptive (ii) puncta that are in contact with dPV soma and dendrite are shown to be in apposition to the postsynaptic marker Homer1 (yellow arrows). Scale bars: 2μm. **B)** Quantification of cutaneous (green) and proprioceptive (yellow) input as percentage of the total sensory input to dPVs (labeled by the intersection used in A). Cutaneous input show higher innervation of dPVs. Mann-Whitney test, **p = 0.0038. **C-D)** 40X confocal image show that

dPVs are directly contacted by Aβ-field (C) and and Aβ-RA (D) LTMRs. Scale bars: 10μm. iii,iv) puncta are shown to be in apposition to Homer1 (yellow arrows). Scale bars: 2μm. **E)** Schematic of conditions for sensory afferent photostimulation**. F)** Representative traces from dPVs showing 10 consecutive sweeps with average oEPSC overlaid of oEPSCs following activation of proprioceptive afferents, Aβ-Field LTMRs, Aβ-RA LTMRs, Aδ-LTMRs, and C-LTMRs. **G)** Grouped data of monosynaptic oEPSC incidence. **H)** Grouped data of monosynaptic oEPSC amplitude. **I)** Schematic summarizing dPV input. **J)** Grouped data showing polysynaptic oEPSC incidence. **K)** Grouped data showing polysynaptic oEPSC amplitude. **L)** Representative trace from dPV showing 10 consecutive sweeps with average overlaid of oEPSCs following activation of CCK+INs. **M)** Grouped data showing oIPSC incidence (left) and representative oIPSC recorded at -20 mV (right). **N)** Representative trace from dPV showing 10 consecutive sweeps with average overlaid of oIPSCs following activation of RORβ+INs. **O)** Representative trace showing 10 consecutive sweeps of sAPs during sensory afferent stimulation (blue bar). Inset shows optically evoked AP. P) Grouped data showing oAP incidence following photostimulation of sensory afferent populations. Q) Histogram of AP probability with a sine wave showing expected sAP frequency overlaid. Raster plot of sAPs across 10 consecutive sweeps with expected sAP frequency shown in grey bars.

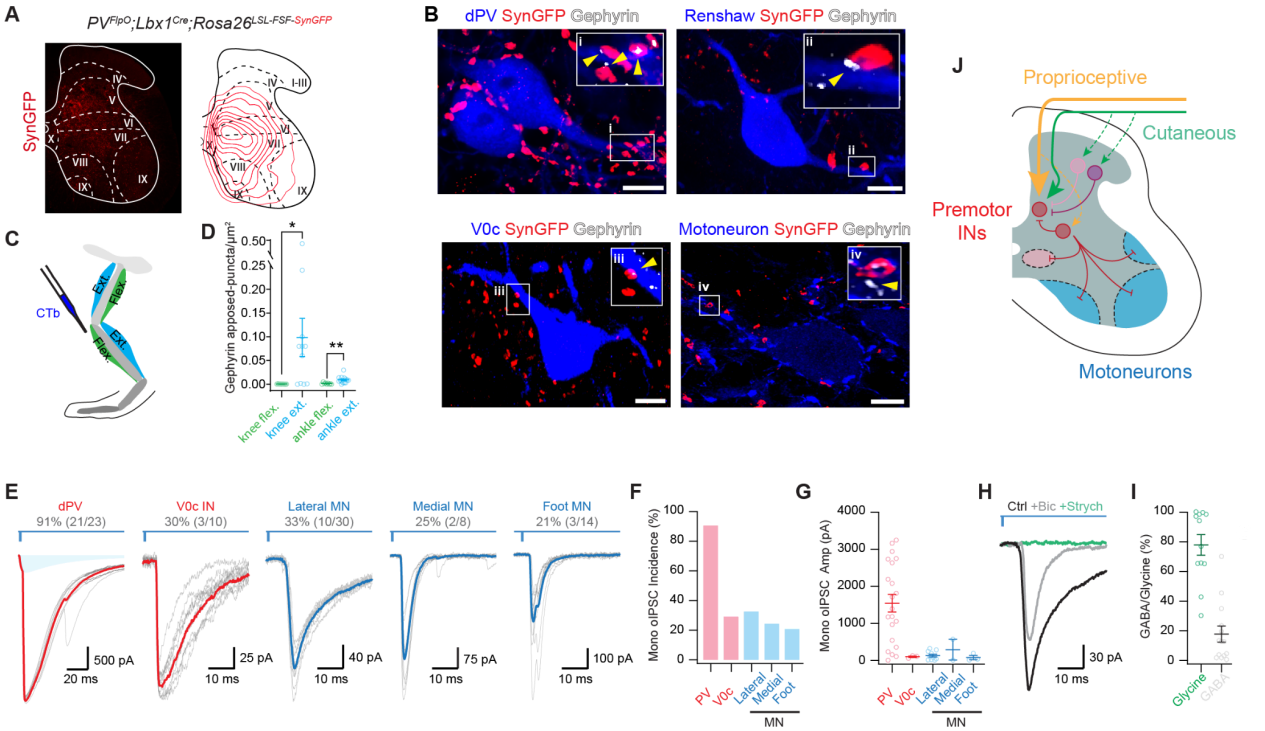

Figure 6. dPVs have diverse postsynaptic circuits. A) Left- representative image from limb level lumbar cord from the intersection *PV*^{FlpO};Lbx^{1Cre};*Rosa*$^{LSL\text{-}FSF\text{-}SynGFP}$ showing dPVs axon terminals in pseudo-red. Right- density map showing the distribution of dPVs axon terminals throughout the dorso-ventral axis of the lumbar spinal cord. **B)** 40x confocal images demonstrating direct contact between dPVs terminals (SynGFP, red) and deep dorsal horn and ventral horn interneurons (blue). dPVs are shown to contact other dPVs (top left, intersection used: *PV*^{FlpO};Lbx^{1Cre};*Rosa*$^{LSL\text{-}FSF\text{-}SynGFP}$;*Rosa*$^{LSL\text{-}FSF\text{-}TdTomato}$), Renshaw cells (top right, stained with Mouse- anti calbindin), V0c interneurons (bottom left, stained with Goat- anti ChAT) and motor neurons (bottom right, stained with Goat- anti ChAT). Scale bar: 10 µm. i,ii,iii,iv) dPVs' terminals are shown to be in apposition to the inhibitory postsynaptic marker Gephyrin (white, yellow arrows). **C)** Diagram of retrograde tracing of flexor and extensor motor neurons experiment. Alexa fluor 555- conjugated Cholera toxin (CTb) was injected into *PV*^{FlpO};Lbx^{1Cre};*Rosa*$^{LSL\text{-}FSF\text{-}SynGFP}$ knee extensor (Vastus Lateralis, VL), knee flexor (biceps femoris, BFP), ankle extensor (lateral gastrocnemius, LG) and ankle flexor (tibialis anterior, TA) to label respective motor neurons. **D)** Quantification of Gephyrin-apposed GFP puncta on motor neurons' soma (normalized to cell body area) shows preferred synaptic input onto hindlimb extensors (Mann whitney test with holm-Sidak correction for multiple comparisons, VL vs BFP *p=0.0094, LG vs TA **0.0003). **E)** Representative traces showing 10 consecutive sweeps with average oIPSC overlaid. Recorded from dPV and V0c interneurons, and Lateral, Medial, and Foot motoneurons following dPV photostimulation. **F)** Grouped data of monosynaptic oEPSC incidence. **G)** Grouped data of monosynaptic oEPSC amplitude. **H)** Representative response of oIPSCs following application of

bicuculline (grey) and strychnine (green). **I)** Grouped data showing the GABA/glycine contribution to oIPSCs. **J)** Schematic summarizing dPV inputs and outputs.

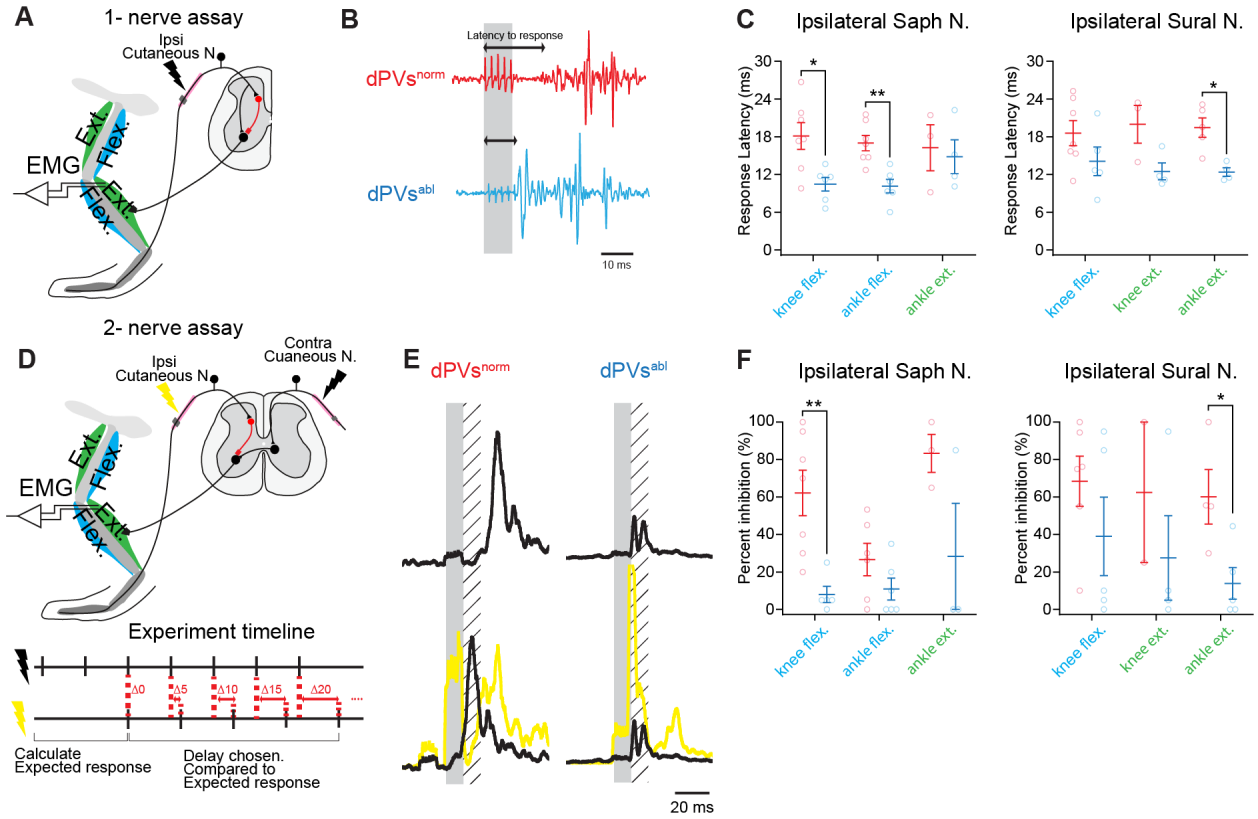

Figure 7. dPVs mediate cutaneous- evoked muscle inhibition. A) Diagram depicting the 1-nerve stimulation assay designed to reveal the contribution of dPVs to motor activity evoked by stimulation of ipsilateral cutaneous nerves. Nerve cuffs were implanted on the right sural nerve and left saphenous nerve. EMG electrodes were implanted into the right and left semitendinosus (St, knee flexor), right vastus lateralis (VL, knee extensor), left tibialis anterior (TA, ankle flexor) and right and left gastrocnemius (Gs, ankle extensor). EMG responses were recorded from hindlimb flexors and extensors following stimulation of cutaneous nerves (saphenous / sural nerve). **B)** Example St EMG responses to stimulation of the right saphenous nerve at 5 times threshold (see methods) in dPV^{norm} (top) and dPV^{abl} (bottom), during the experiment described in D. **C)** Latency to response to stimulation of the saphenous (left) or sural (right) nerves of ipsilateral hindlimb muscles during the experiment depicted in D. **D)** Top- diagram of the 2-nerve stimulation assay applied to reveal if dPVs mediate sensory-evoked ipsilateral inhibition. Bottom- experiment timeline. Nerve cuffs and EMG electrodes were placed as in D. Stimulation of the contralateral cutaneous nerve (saphenous/ sural) alone (black lightning) was used to calculate the expected response in the absence of sensory evoked ipsilateral inhibition. Following, both nerves were stimulated (yellow lightning), with variable delays and compared to the expected response to reveal ipsilateral inhibition. **E)** Top- expected Gs EMG response to stimulation of a single cutaneous nerve in dPV^{abl} (left) and dPV^{norm} (right),

averaged over 20 responses. Bottom- expected responses (black) superimposed on single trial responses to stimulation of both cutaneous nerves (yellow). Left- response to stimulation of both nerves (15 ms delay), shows a “dip” that is absent in the expected response, indicating ipsilateral inhibition. Right- no “dip” is seen (0 ms delay), suggesting a loss of inhibition. For each mouse and each muscle, the delay in which responses were best aligned was chosen for further analysis. **F)** Percent inhibition (the percentage of trials where inhibition was detected) in hindlimb muscles, mediated by ipsilateral saphenous (left) and ipsilateral sural (right) nerves, following the experiment in G. Statistical analysis was done using Mann Withney test, with *$p < 0.05$ and **$p < 0.005$. Graphs show average +S.E.M. blue and red denote dPV^{norm} and dPV^{abl}, respectively.